Deletion of *Serf2* shifts amyloid conformation in an Aβ amyloid mouse model

E. Stroo[1*], L. Janssen[1*], O. Sin[1], W. Hogewerf[1], M. Koster[2], L. Harkema[2], S.A. Youssef[2,3], N. Beschorner[4], A.H.G. Wolters[5], B. Bakker[1], A. Thathiah[6,7], F. Foijer[1], B. van de Sluis[2], J. van Deursen[8], M. Jucker[4], A. de Bruin[2,3], E.A.A. Nollen[1]

[1]European Research Institute for the Biology of Ageing, University of Groningen, University Medical Centre Groningen, The Netherlands

[2]Department of Biomolecular Health Sciences, Faculty of Veterinary Medicine, Utrecht University, The Netherlands

[3]Department of Pediatrics, Molecular Genetics Section, University of Groningen, University Medical Centre Groningen, The Netherlands

[4]Department of Cellular Neurology, Hertie-Institute for Clinical Brain Research, University of Tübingen, Tübingen, Germany.

[5]Department of Biomedical Sciences of Cells and Systems, University Medical Centre Groningen, The Netherlands

[6]VIB Center for the Biology of Disease, KU Leuven Center for Human Genetics, University of Leuven, Leuven, Belgium

[7] Department of Neurobiology, University of Pittsburgh Brain Institute, University of Pittsburgh School of Medicine, Pittsburgh, PA USA

[8]Mayo Clinic, United States of America

*These authors contributed equally

[#]Correspondence: e.a.a.nollen@umcg.nl

Keywords: Small EDRK-rich factor 2, SERF, protein aggregation, amyloid-beta, amyloid polymorphisms

25 **Highlights**

26 - Loss of SERF2 slows embryonic development and causes perinatal lethality
27 - SERF2 affects proliferation in a cell-autonomous fashion
28 - Brain-specific *Serf2* knockout does not affect viability or Aβ production
29 - Brain deletion of *Serf2* shifts the amyloid conformation of Aβ

Abstract

Neurodegenerative diseases like Alzheimer, Parkinson and Huntington disease are characterized by aggregation-prone proteins that form amyloid fibrils through a nucleation process. Despite the shared β-sheet structure, recent research has shown that structurally different polymorphs exist within fibrils of the same protein. These polymorphs are associated with varying levels of toxicity and different disease phenotypes. MOAG-4 and its human orthologs SERF1 and SERF2 have previously been shown to modify the nucleation and drive amyloid formation and protein toxicity *in vitro* and in *C. elegans*. To further explore these findings, we generated a *Serf2* knockout (KO) mouse model and crossed it with the *APPPS1* mouse model for Aβ amyloid pathology. Full-body KO of *Serf2* resulted in a developmental delay and perinatal lethality due to insufficient lung maturation. Therefore, we proceeded with a brain-specific *Serf2* KO, which was found to be viable. We examined the Aβ pathology at 1 and 3 months of age, which is before and after the start of amyloid deposition. We show that SERF2 deficiency does not affect the production and overall Aβ levels. *Serf2* KO-*APPPS1* mice displayed an increased intracellular Aβ accumulation at 1 month and a higher number of Aβ deposits compared to *APPPS1* mice with similar Aβ levels. Moreover, conformation-specific dyes and electron microscopy revealed a difference in the structure and amyloid content of these Aβ deposits. Together, our results reveal that SERF2 causes a structural shift in Aβ aggregation in a mammalian brain. These findings indicate that a single endogenous factor may contribute to amyloid polymorphisms, allowing for new insights into this phenomenon's contribution to disease manifestation.

50 **Introduction**

51 Protein aggregation is a pathological hallmark shared by several age-related neurodegenerative
52 diseases, such as Alzheimer (AD), Parkinson and Huntington disease. The amyloid-like aggregates
53 that accumulate in each of these diseases are composed of disease-specific proteins, i.e., amyloid-beta
54 (Aβ) and tau in AD[1–4], alpha-synuclein (α-Syn) in Parkinson disease[5] and Huntingtin (HTT) in
55 Huntington disease[6]. While the exact molecular mechanisms underlying the disease pathology remain
56 to be elucidated, genetic evidence indicates that these aggregation-prone proteins play a key role in the
57 disease processes. In AD multiple causative mutations have been found in three genes: the amyloid
58 precursor protein (*APP*)[7–15], presenilin-1 (*PSEN1*)[16–20] and presenilin-2 (*PSEN2*)[21–24] (for a full list of
59 known AD-linked mutations see https://www.alzforum.org/mutations). The *APP* gene encodes the
60 precursor protein from which Aβ is produced through sequential cleavage by a β- and γ-secretase. The
61 *PSEN* genes encode the main catalytic subunit of the γ-secretase complex. The fact that all the
62 causative mutations affect the production, length and/or structure of the Aβ peptides and are sufficient
63 to cause the disease[7,9,29–35,13,14,18,24–28], is arguably the strongest piece of evidence for the involvement
64 of Aβ in the disease process. Causative mutations generally affect the Aβ peptide in one of three ways:
65 (i) an overall increase in Aβ production[9,36], (ii) a shift in the production of shorter variants, like $A\beta_{40,}$
66 to more aggregation-prone, longer variants, like $A\beta_{42}$ (or $A\beta_{43}$)[18,31,37–39], (iii) Aβ peptides with a
67 modified core region, resulting in an increased propensity for aggregation[35,40–42]. Taken together,
68 these mutations do not necessarily increase the amount of Aβ, but rather increase the
69 likelihood of Aβ aggregation. Similarly, several mutations in the *SNCA* gene that have been linked
70 to Parkinson disease have been shown to alter α-Syn aggregation[43–48]. In Huntington disease, any
71 expansion of a polyglutamine stretch in the *HTT* gene that exceeds 36 repeats has been shown to
72 facilitate HTT aggregation and cause the disease[49]. Hence, changes in the folding and aggregation of
73 these disease proteins are believed to be at the basis of the observed pathology. In addition, there is
74 increasing evidence that distinct structural variants exist between aggregates of the same disease
75 protein and that these polymorphs are associated with varying degrees of toxicity[50–58] . For instance,
76 recent studies with brain samples from human AD patients have shown that variations in the disease

type and disease progression correlate with the presence of structurally different aggregates and fibrils[59–62]. The knowledge that small changes in the structural conformation of these aggregates can have far-reaching effects on the disease manifestation could provide a new avenue for the development of therapeutics. Until now, most research into potential treatments of AD has focused on either reducing the overall amount of aggregating proteins or preventing aggregation, not modifying the aggregation process.

In a previous study, our group performed a genetic screen in *Caenorhabditis elegans* (*C. elegans*) and identified a small, intrinsically disordered protein of unknown function with the capacity to modify protein aggregation and to enhance the resulting toxicity of multiple disease-related, aggregation-prone proteins[63]. This peptide was dubbed *mo*difier of *ag*gregation-4 (MOAG-4) and was found to be an ortholog of two human genes: *Serf1A* and *Serf2*. Both SERF1A and SERF2 were shown to exacerbate protein aggregation and toxicity in human neuroblastoma and HEK293 cell lines as well[64]. *In vitro* assays with MOAG-4 and SERF1A have demonstrated that these proteins can specifically accelerate the aggregation kinetics of amyloidogenic proteins, but do not affect aggregation of non-amyloidogenic proteins[65,66]. For α-Syn, this amyloid-promoting effect has been shown to depend on the transient interaction of these positively-charged peptides with negatively-charged regions and the disruption intramolecular electrostatic interactions within the protein[65,67,68]. Removal of MOAG-4 or SERF from a biological system did not change the overall levels of the aggregation-prone proteins or activate chaperone pathways known to suppress aggregation[64]. Therefore, the reduced toxicity would appear to rely solely on the structural shift in the aggregation process[64,65]. In this study, we investigate whether the removal of SERF2 modifies the aggregation of Aβ in the biologically more complex environment of the mammalian brain.

99 **Results**

100 *Full-body Serf2 KO results in developmental delay and perinatal lethality in mice*

101 To establish the role of SERF2 *in vivo*, full-body *Serf2* knockout (KO) mice were generated (Figure
102 S1A-C). During an initial cross, using the four homozygous *Serf2* KO animal (*Serf2*$^{-/-}$) and eight
103 heterozygous *Serf2* KO animals (*Serf2*$^{+/-}$) we obtained, only one *Serf2*$^{-/-}$ survived the day of birth
104 compared to 27 *Serf2*$^{+/-}$ and 96 *Serf2* wild-type (*Serf2*$^{+/+}$) mice (Supplemental Table 1). After
105 backcrossing into C57BL/6J background, interbreeding of *Serf2*$^{+/-}$ animals did not result in any viable
106 *Serf2*$^{-/-}$ mice at the time of weaning (Figure 1A,1B). To determine whether *Serf2*$^{-/-}$ mice died during
107 fetal development, we examined the offspring at multiple developmental stages: embryonic day 13.5,
108 15.5 and 17.5. In all of the examined embryonic stages we observed the expected Mendelian ratio of
109 genotypes, around 25 % *Serf2*$^{+/+}$ and *Serf2*$^{-/-}$ embryos and around 50 % *Serf2*$^{+/-}$ (Chi Square: E13.5
110 p=0.9672; E15.5 p= 0.4432; E17.5 p=0.7674) (Figure 1B). At birth (P0), all *Serf2*$^{-/-}$ displayed
111 respiratory distress and the majority (5/7) died within 30 minutes of being born. At the time of
112 weaning, the Mendelian ratio was maintained between the *Serf2*$^{+/+}$ and *Serf2*$^{+/-}$ animals, but no *Serf2*$^{-/-}$
113 mice survived until this stage (Chi Square: P22 p<0.0001) . Examination of *Serf2* mRNA expression at
114 E13.5 showed a 50 % reduction for *Serf2*$^{+/-}$ and complete KO for *Serf2*$^{-/-}$ compared to *Serf2*$^{+/+}$ (One-
115 way ANOVA: *Serf2*$^{+/-}$ and *Serf2*$^{-/-}$ vs *Serf2*$^{+/+}$ p_{Bon}<0.0001) (Figure 1C). A similar ratio in SERF2
116 expression was also observed on the protein level (Figure 1D). The *Serf1* mRNA levels were not
117 affected by the change in *Serf2* levels, indicating there is no compensatory mechanism between these
118 genes (One-way ANOVA: p=0.2403) (Figure 1C). Further analysis of the *Serf2*$^{-/-}$ embryonic
119 phenotype revealed a reduction in embryo size of *Serf2*$^{-/-}$ compared to *Serf2*$^{+/+}$ and *Serf2*$^{+/-}$ from E15.5
120 until birth (Two-way ANOVA: E17.5 WT vs KO p_{bon}<0.05; P0 WT vs ko p_{Bon}<0.0001) (Figure 1E,
121 S1D-E). No differences in size could be observed between *Serf2*$^{+/+}$ and *Serf2*$^{+/-}$ embryos during the
122 embryonic stage leading up to birth (P0). Histological examination of various tissues revealed a
123 developmental delay of approximately one to two days in the organs of E17.5 *Serf2*$^{-/-}$ embryos
124 compared to the previous time points and standard embryonic development[69,70]. This was most
125 prominently in the lungs, through reduced expansion of alveoli and augmented tissue density, and in

126 the kidneys, by the increased amount of mesenchyme between the tubules and glomeruli (Figure S1F).
127 At the time of birth, the lungs of *Serf2*$^{-/-}$ pups displayed a significantly reduced saccular space (t-test:
128 p= 0.0088) (Figure 1F), reflecting insufficient lung expansion and maturation. This partial fetal
129 atelectasis seems to explain the observed respiratory distress and a likely cause of the perinatal
130 lethality in *Serf2*$^{-/-}$ pups. Placental abnormalities have been shown to cause impaired transfer of
131 nutrients and oxygen to the embryo, resulting in growth delays[71]. To exclude this as a potential cause,
132 we examined the placenta at all three embryonic stages for microscopic lesions in the placental
133 labyrinth or other changes. No genotype-related pathology could be found, indicating that absence of
134 SERF2 in the embryo itself is responsible for the observed growth phenotype. This seems to be
135 supported by the fact that CRISPR-induced *Serf2*$^{-/-}$ clones of HEK293T cells display a delay in
136 proliferation (Figure S2A). Moreover, RNA sequencing analysis of mouse embryonic fibroblasts
137 (MEF) isolated from E13.5 embryos showed a clear enrichment of GO-terms clustered around three
138 closely related biological functions: cell cycle, cell proliferation and cell adhesion (Supplemental
139 Figure S2A-B). Interestingly, in the cell cycle cluster we observe an overall upregulation of factors
140 driving cell division and downregulation of growth arrest factors in *Serf2*$^{-/-}$ MEFs (Supplemental Table
141 2). This observation seems in line with a developmental delay phenotype in *Serf2*$^{-/-}$ mice, because it is
142 known that cell proliferation is favored over differentiation in earlier stages of embryonic development
143 compared to later stages[72]. Overall, the cell culture results point towards a cell-autonomous effect of
144 SERF2 and suggest that loss of *Serf2* results in delayed growth. While our previous study also
145 demonstrated a cell-autonomous function for moag-4, it did not show any effects of moag-4 deletion
146 on the viability, life span or size of *C. elegans*[64]. All together, our results suggest that *Serf2* KO causes
147 delayed maturation of certain organs at the time of birth resulting in death. Given the cell-autonomous
148 nature of the effects of SERF2, we aimed to avoid these adverse effects by creating an organ-specific
149 conditional KO model.

150 *Brain-specific KO of Serf2 does not affect viability or the Aβ production pathway*

151 To study the effect of *Serf2* KO on amyloid pathology in the brain, we circumvented the perinatal
152 lethality of full-body *Serf2* KO mice by generating a brain-specific *Serf2* KO mouse model (*Serf2*$^{br-/-}$).

153 The conditional KO was obtained by combining our *Serf2*$^{flox/flox}$ mice with a *Sox1-Cre* model[73] (Figure
154 S3A). SOX1 is one of the earliest transcription factors expressed in neuronal precursors of the
155 ectoderm from embryonic day 7.5[74,75]. Consequently, the *Sox1* promotor was selected as a pan-
156 neuronal driver of Recombinase cre expression to restrict homologous recombination to the central
157 nervous system[76]. Analysis of *Serf2* expression on the mRNA and protein level in various organs
158 confirmed brain-specific ablation of *Serf2* by *Sox1*-mediated *Cre* expression in our *Serf2*$^{flox/flox}$ mice (t-
159 test WT vs *Serf2*$^{br-/-}$ brain: 1m p=0.0022; 3m p=0.00527) (Figure S3B-C). This conditional KO was
160 crossed with the *APPPS1-21* amyloid (AM) model[77], which contains human transgenes for both APP
161 with the Swedish KM670/671NL mutation and PSEN1 with the L66P mutation. From this cross we
162 obtained four experimental groups: WT, *Serf2*$^{br-/-}$, AM and AM;*Serf2*$^{br-/-}$ (Figure 2A). Upon crossing
163 of the *Serf2*$^{br-/-}$ with the amyloid model, we observed the expected Mendelian ratio for all the
164 genotypes at P22, indicating that the viability is not significantly affected by brain-specific KO of
165 *Serf2* (Chi Square: p= 0.37)(Supplemental Table 3). Based on the known progression of Aβ plaque
166 pathology in the AM mice, we selected two age groups for further analysis: before (1 month) and after
167 (3 months) Aβ plaque deposition (Figure 2B). Analysis of the *Serf2* mRNA levels in both age groups
168 showed that *Serf2* expression was not altered by the plaque pathology and confirmed the KO in the
169 *Serf2*$^{br-/-}$ and AM;*Serf2*$^{br-/-}$ mice. Some residual *Serf2* expression could be detected in the brains of the
170 KO groups likely due to the presence of cells from non-neuronal lineage in the samples, e.g. cells from
171 circulatory system (Two-way ANOVA: *Serf2*$^{br-/-}$ and AM;*Serf2*$^{br-/-}$ vs WT 1m p_{bon} <0.001; 3m p_{bon}
172 <0.0001) (Figure 2C). These results were also confirmed on the protein level using western blot
173 (Figure 2D). In accordance with the effects observed in the full-body *Serf2*$^{-/-}$ mice, the *Serf2*$^{br-/-}$ and the
174 AM;*Serf2*$^{br-/-}$ mice did show a reduction in brain weight compared to WT in both age groups (Two-
175 way ANOVA: *Serf2*$^{br-/-}$ vs WT both ages p_{bon}<0.01; AM;*Serf2*$^{br-/-}$ vs WT 1m p_{bon}<0.0001; 3m
176 p_{bon}<0.001) (Figure 2E). While the weight reduction seems to be slightly more pronounced in
177 AM;*Serf2*$^{br-/-}$ compared to *Serf2*$^{br-/-}$, AM by itself displayed no significant change in brain weight. This
178 would indicate that *Serf2* ablation, *Cre* expression or a combination of both is most likely responsible
179 for the difference in weight. However, AM mice may be more susceptible to this effect (Figure 2E).
180 To distinguish between the effects of *Cre* expression and *Serf2* KO, we also examined the *Sox1-Cre*

181 mice[76] without floxed *Serf2* (*Cre*^{br}) and crossed them with *APPPS1-21*[78] without floxed *Serf2*. The
182 *Cre*^{br} mice also showed a reduction in brain weight compared to the WT controls, which was more
183 pronounced at 1 month (One-Way ANOVA: *Cre*^{br} vs WT 1m $p_{bon}<0.05$) (Figure S3D), but was overall
184 less extensive than the reduction in *Serf2*$^{br-/-}$ animals (One-way ANOVA: *Cre*^{br} vs WT $p_{bon}<0.01$;
185 AM;*Cre*^{br} vs WT $p_{bon}<0.001$) (Figure 2F). Together, this suggests that *Cre* expression is partially
186 responsible for the observed decrease in brain size, particularly at 1 month of age. Due to ongoing
187 brain maturation between 1 and 3 months, all groups show a significant increase in brain weight (Two-
188 way Anova: Age $p<0.0001$), but this maturation appeared unaffected by *Serf2* KO. Moreover, the
189 difference in brain weight between WT and *Serf2*$^{br-/-}$remained constant beyond the age of 3 months up
190 to 11 months of age (Figure S3E). This suggests that the reduction in brain size takes place during
191 specific stages of brain development, but that the continued development is not necessarily altered by
192 these changes. Additional histological examination of the brains with hematoxylin-eosin staining
193 revealed no difference in the cell density (Figure 2G), nor did we find any evidence of degeneration,
194 apoptosis or necrosis. Apart from the overall reduction in weight, the brains showed no structural
195 abnormalities and the tissue appeared healthy.

196 Next, we examined whether the brain KO of *Serf2* affected any of the key components in the Aβ
197 aggregation process, like altering the levels of APP or the production of its cleavage products, $A\beta_{40}$
198 and $A\beta_{42}$. We determined the expression of human *APP* in WT, *Serf2*$^{br-/-}$, AM and AM;*Serf2*$^{br-/-}$ mice
199 at both 1 and 3 months of age and observed no difference due to brain specific *Serf2* KO (t-test: 1m
200 p=0.9170; 3m p=0.9963) (Figure 2H, data from WT, *Serf2*$^{br-/-}$ not included due to lack of APP
201 construct and absence of signal). Western blot analysis confirmed there was also no difference in APP
202 protein levels between AM and AM;*Serf2*$^{br-/-}$ (t-test: 1m p= 0.1157;3m p=0.5908) (Figure 2I and J).
203 Further analysis of $A\beta_{40}$ (Two-way ANOVA: Genotype p=0.8841; Age $p<0.0001$;Interaction
204 p=0.8841) (Figure 2K) and $A\beta_{42}$ (Two-way ANOVA: Genotype p=0.7006; Age $p<0.0001$;Interaction
205 p=0.6522) (Figure 2L) showed an increase in concentration between 1 and 3 months, but this was the
206 same in both AM and AM;*Serf2*$^{br-/-}$. Given the variability in the Aβ concentrations at 3 months and the
207 fact that the ratio between these two peptides is known to affect the aggregation process, we also

208 investigated the correlation between these two Aβ levels (Figure 2M). This analysis showed that mice
209 with a high $A\beta_{42}$ concentration display a similarly high $A\beta_{40}$ level, maintaining a comparable $A\beta_{40}$
210 /$A\beta_{42}$ ratio for both AM and AM;*Serf2*$^{br-/-}$ animals. Taken together, this data suggests that SERF2 does
211 not affect the levels of APP and its cleavage products, $A\beta_{40}$ and $A\beta_{42}$. These findings are in accordance
212 with the previously observed effects of MOAG-4 on the aggregation of polyglutamine, Aβ and αSyn
213 in *C. elegans*, which modifies the aggregation process without changing the overall levels of these
214 aggregation-prone proteins[64]. While the difference in brain size is definitely a factor to be considered
215 during further analysis, given the fact that we observed no obvious changes in the overall health,
216 continued development and APP processing pathway of these brain-specific *Serf2* KO mice, we
217 proceeded with our analysis of Aβ pathology in these animals.

218 *Serf2 KO alters the amount of Aβ deposition in the brain*

219 We next investigated whether SERF2 affects the Aβ aggregation by performing immunohistological
220 analysis of the Aβ plaque pathology. Initially, we performed a general Aβ staining using the 6E10
221 antibody. In accordance with the known progression of Aβ plaque pathology in the amyloid model, we
222 only found extracellular deposits in the 3-month-old AM and AM;*Serf2*$^{br-/-}$ mice. As expected, most
223 plaques were found in the cortex, with some pathology beginning to spread to the hippocampus as
224 well (Figure S4). Microscopic inspection of the Aβ deposits revealed a broad range of sizes with a
225 wide variety in staining intensity and patterns, but we found no clear morphological differences
226 between the plaque population found in AM and AM;*Serf2*$^{br-/-}$ (Figure 3A, S4). Quantification of the
227 6E10-positive deposits showed a slight increase in AM;*Serf2*$^{br-/-}$ compared to AM, but this just failed
228 to reach statistical significance in the Bonferroni corrected post-hoc comparison (Two-way ANOVA:
229 all 3m non-AM vs AM groups $p_{bon} < 0.0001$; AM vs AM;*Serf2*$^{br-/-}$ $p_{bon} = 0.063$)(Figure 3B). Given the
230 high variability in plaque load between animals within the same experimental group, we examined
231 whether this variability reflected the previously observed variation in Aβ levels. Unsurprisingly,
232 animals with higher levels of $A\beta_{40}$ (Figure 3C) and $A\beta_{42}$ (Figure 3D) displayed a higher overall plaque
233 load in both groups. More interestingly, our linear regression analysis revealed that AM;*Serf2*$^{br-/-}$ mice
234 tend to have a significantly higher plaque load than AM mice with similar Aβ levels (Supplemental

235 Table 4). A second general Aβ stain with the W0-2 antibody displayed a similar slight increase in the
236 amount of plaque deposits in AM;*Serf2*$^{br-/-}$ at 3 months (Two-way ANOVA: all 3m non-AM vs AM
237 groups p_{bon} <0.0001; AM vs AM;*Serf2*$^{br-/-}$ p_{bon} =0.101) (Figure 3E). In fact, a comparison between the
238 6E10 and the W0-2 staining in individual animals confirmed the similarity between both staining
239 patterns at 3 months (Figure 3F, S5, Supplemental Table S3). Interestingly, our detection algorithm
240 also picked up a small increase in the counts of W0-2-positive foci in the 1 month AM;*Serf2*$^{br-/-}$ group
241 (Two-way ANOVA: 1m WT vs AM;*Serf2*$^{br-/-}$ p_{bon} =0.088 ; *Serf2*$^{br-/-}$ vs AM;*Serf2*$^{br-/-}$ p_{bon} =0.081; AM
242 vs AM;*Serf2*$^{br-/-}$ p_{bon} =0.127; all other comparisons p_{bon} >0.999) (Figure 3E). Closer examination of the
243 microscopic images revealed the identified spots were not extracellular plaques, but were the result of
244 increased levels of W0-2-positive intracellular staining in AM;*Serf2*$^{br-/-}$ (Figure S7A). Some low level
245 intracellular W0-2 and 6E10 staining could also be observed in the other 1-month-old AM mice, but
246 not to the extent that it was picked up by the detection algorithm (Figure S7A-B). This would suggest
247 that the deletion of *Serf2* already alters the intracellular accumulation of Aβ prior to plaque deposition.
248 Overall, these results indicate that the presence of SERF2 is indeed able to modify Aβ aggregation in
249 the mouse brain.

250 *SERF2 deficiency changes the proportion of ThS-positive cores, but not the immunoreactivity*
251 *of deposits*

252 To investigate if SERF2 also affected the amount of Thioflavin-positive fibrils, we performed
253 Thioflavin-S (ThS) staining. Here, we again observed a large variety in the amount of ThS-positive
254 plaques between individual animals, but we found no mean difference between AM and AM;*Serf2*$^{br-/-}$
255 mice (Two-way ANOVA: all 3m non-AM vs AM groups p_{bon} <0.001) (Figure 3G). However, further
256 analysis of the correlation between Aβ levels and the amount of ThS-positive plaques revealed that
257 AM mice showed a positive correlation similar to the general Aβ stainings, while AM;*Serf2*$^{br-/-}$ mice
258 displayed an inverse relationship (Figure 3H, 3I, Supplemental Table S3). Consequently, a general
259 increase in Aβ deposits does not equate to an increase in amyloid deposition in AM;*Serf2*$^{br-/-}$ mice, as
260 it does in AM mice (Figure 3J), further demonstrating a change in the amyloid formation in *Serf2* KO
261 mice. In addition, we investigated microglia activation and whether we could detect a change in the

262 gliosis associated with Aβ plaques. Staining for Iba1 showed a slight increase in the AM;*Serf2*$^{br-/-}$ mice
263 compared to AM (Two-way ANOVA: 3m non-AM groups vs AM p_{bon} <0.01; non-AM groups vs
264 AM;*Serf2*$^{br-/-}$ p_{bon} <0.0001; AM vs AM;*Serf2*$^{br-/-}$ p_{bon} <0.01) (Figure 3K), similar to what was observed
265 with the 6E10 staining (Figure 3B). We therefore examined if this increase was simply related to the
266 increase in Aβ deposits or if AM;*Serf2*$^{br-/-}$ also displayed a different immune response to plaques
267 compared to AM. Our analysis revealed a similar correlation between 6E10-positive deposits and
268 immune response for AM and AM;*Serf2*$^{br-/-}$ mice, suggesting the deposits evoked a similar immune
269 response in both groups(Figure S6A, Supplemental Table S3).

270 *Knockout of Serf2 changes the plaque composition and fibril structure*

271 Given the differences in the reactivity of the Aβ deposits between the various stains, we decided to
272 explore the composition within the individual plaques in greater detail. To this end, we made use of
273 two luminescent conjugated oligothiophenes (LCO), qFTAA (quadro-formylthiophene acetic acid)
274 and hFTAA (hepta-formylthiophene acetic acid). These LCOs are small hydrophobic ligands with a
275 high affinity for binding distinct types of amyloids and can easily be distinguished from each other
276 based on their spectral properties[79]. The smallest of the two molecules, qFTAA, is characterized by a
277 peak in its emission spectrum around 500 nm and has been shown to stain compact, multifilament
278 fibril structures, coinciding with ThT and Congo red staining[80–82]. Whereas hFTAA emits in the
279 yellow to red range with a peak around 600 nm and is capable of staining prefibrillar (non-
280 thioflavinophilic) and single fibril aggregates found during the lag-phase of in vitro ThT kinetics
281 (Figure 4A). The prefibrillar aggregates were shown to be stained with 6E10, but not Congo red, ThT
282 or qFTAA[80,82,83]. Previous studies have shown that by combining LCO dyes it is possible to uncover
283 structural differences in plaque composition[83–85]. We performed confocal spectral imaging of
284 randomly selected plaques in 3-month-old AM and AM;*Serf2*$^{br-/-}$ mice after double staining with both
285 LCOs and determined the ratio of the light intensity emitted at 502nm and 588nm as a measure for the
286 relative amounts of fibrillar and prefibrillar aggregates within the individual plaques. An exploratory
287 frequency analysis of the intensity ratios found in both groups revealed a three-peak pattern in which
288 the middle peak was similarly represented in both groups (Figure 4B, green area). The first peak,

289 however, was predominantly found in AM mice (Figure 4B, red area), while the third peak was mainly
290 detected in AM;*Serf2*$^{br-/-}$ (Figure 4B, blue area). This shift in ratio was also reflected by a significant
291 difference in the average intensity ratio between AM and AM;*Serf2*$^{br-/-}$ (t-test $p<0.001$) (Figure 4C).
292 This increase in intensity ratio could not be observed in AM;*Cre*^{br} mice (t-test $p=0.6047$) (Figure 4C,
293 insert), indicating that this effect is caused by the *Serf2* KO and unrelated to *Cre* expression. Given the
294 fact that AM;*Cre*^{br} animals also show a decrease in brain weight without a change in LCO staining,
295 this would also suggest that the weight reduction is not a factor in these results. Although, as the
296 change in brain weight is more pronounced in *Serf2*$^{br-/-}$ animals, we cannot completely exclude this as
297 a potential contributing factor. Next, we examined if the change in the intensity ratio correlated with
298 the slight increase in 6E10-positive deposits we observed in AM;*Serf2*$^{br-/-}$ (Figure 4D). However, the
299 higher average intensity ratio in AM;*Serf2*$^{br-/-}$ mice was not related to this general plaque load nor the
300 number of W0-2- or ThS-positive deposits (Figure S6B, S6C). Further microscopic analysis of low
301 intensity ratio deposits from AM mice showed a plaque with a qFTAA- and hFTAA-positive core and
302 a border that was only stained by hFTAA (Figure 4E, left panels). The high intensity ratio deposits
303 from AM;*Serf2*$^{br-/-}$ mice, on the other hand, revealed a qFTAA-positive core, but virtually no hFTAA-
304 staining (Figure 4E, right panels), demonstrating the difference in plaque composition reflected by the
305 shift in LCO intensity ratios. Additionally, we visualized the global fibrillar structure of the plaques on
306 a nanometer scale using high resolution, scanning transmission electron microscopy (STEM). Overall,
307 STEM images of plaques from AM;*Serf2*$^{br-/-}$ tended to show more condensed plaques composed of
308 short, thick and densely packed bundles of fibers with little space in between (Figure 4F, right panels).
309 In the AM mice, however, the plaques we observed displayed more loosely packed fibrils (Figure 4F,
310 left panels). Taken together, these findings suggest *Serf2* KO in mice leads to a shift in the Aβ
311 aggregation process, resulting in an altered structural composition of the plaques.

312 **Discussion**

313 Previous studies identified MOAG-4 and its human orthologs SERF1A and SERF2 and their potential
314 to modify the aggregation of amyloidogenic proteins. While the exact endogenous biological function
315 of these peptides remains unclear, a recent study has provided evidence for RNA-binding properties of

316 SERF1A through a region which is highly conserved in MOAG-4 and SERF2[86]. In this study, we have
317 demonstrated in cells and mice that SERF2 provides a growth advantage during development. The
318 absence of SERF2 or MOAG-4 in itself does not appear to be lethal in cells, worms or the brain-
319 specific KO mice. Therefore, we postulate that the observed perinatal lethality in the full-body KO
320 mice is a secondary effect of the delay in growth due to insufficient maturation of certain organs at
321 birth. This appears to be supported by the fact that some pups survived the initial minutes after birth
322 and incomplete penetrance of the lethality in the earliest generations with mixed genetic background.
323 The 129SV genetic background present in these mice is known to have a gestation period that is on
324 average around one day longer than C57/Bl6J mice[87], which could result in improved lung maturation.
325 While the exact function of SERF2 remains unknown, we propose its effects on growth and
326 development are most likely caused through one of two mechanisms: either SERF2 facilitates cell
327 proliferation or it protects cells from stressors that create an unfavorable environment for cell division.
328 In the latter case, we would expect to see an upregulation of stress pathways or cell cycle arrest
329 proteins inhibiting the cell cycle in *Serf2*$^{-/-}$ cells. Interestingly, the RNA seq analysis of the MEFs from
330 our *Serf2*$^{-/-}$ mice showed the exact opposite. Cell cycle driving factors were upregulated (e.g. cyclins).
331 Whereas, stress signaling and cell cycle inhibiting factors were downregulated (e.g. GADD45 and
332 GAS1). Thus, the *Serf2*$^{-/-}$ cells actually displayed an increased stimulation of cell proliferation
333 mechanisms, which would fit with cells from earlier stages of embryonic development. This would
334 suggest the first mechanism, with a beneficial role for SERF2 in the efficient execution of cell
335 proliferation, as the most likely explanation for the observed growth effect. Furthermore, an increase
336 in cellular stress would most likely result in decreased health and fitness. However, *moag-4* deletion
337 worms showed no changes in life span compared to controls[64] and, apart from the initial growth
338 deficit, the tissues of *Serf2* KO mice appeared healthy and continued to develop similarly to controls
339 after birth. A recent study showed SERF1a might play a role as an RNA-organizing protein, which
340 localizes to membraneless nuclear organelles, like the nucleolus, under normal physiological
341 conditions. However, under stress conditions, it was shown to migrate to the cytoplasm, where it could
342 drive amyloid toxicity.[88] While there was no compensatory upregulation of SERF1 in response to
343 SERF2 KO and a similar mode of action remains to be demonstrated for SERF2, the structural

344 homology of the two proteins would suggest a comparable function. Given the importance of
345 nucleolar disassembly and reassembly in cell cycle control[89,90], an RNA-organizing function could
346 explain how SERF2 facilitates cell proliferation. This developmental role would have limited
347 biological importance in non-proliferating, differentiated cells, like the brain's neurons or the cells of
348 adult *C. elegans*, and might also explain why we saw no adverse effects in the *moag-4* deletion worms
349 or our adult *Serf2*$^{br-/-}$ mice. While a reduced biological importance of SERF2 later in life could prove
350 interesting with regard to the treatment of age-related neurodegenerative disorders, further exploration
351 of SERF2's endogenous function and how it evolves with ageing will be needed to fully assess this
352 mechanism's therapeutic potential.

353 In this study, we confirmed the ability of SERF2 to modify the Aβ pathology *in vivo* in a mouse model
354 without changing the overall Aβ levels. We showed that mice lacking SERF2 were more prone to
355 form Aβ deposits and that the composition of these deposits was structurally different. In AM mice
356 higher levels of Aβ result in an increase in the numbers of Aβ deposits as well as an increase in the
357 number of ThS-positive deposits. AM;*Serf2*$^{br-/-}$ mice, on the other hand, also show an increase in Aβ
358 deposits, but this did not lead to higher numbers of ThS-positive plaques, indicating an altered
359 dynamic for amyloid formation. These findings were further corroborated by the LCO spectra, which
360 revealed that the plaques in AM;*Serf2*$^{br-/-}$ mice have a different conformation of pre-fibrillar and
361 fibrillar Aβ compared to AM mice. Finally, STEM imaging also confirmed a globally altered structure
362 of the amyloid fibrils in the plaques. Amyloid fibrils are formed through a nucleated self-assembly
363 process characterized by a structural conformation to a β-strand secondary structure and the formation
364 of a critical nucleus during the initial oligomerization. The nuclei act as seeds from which the fibrils
365 grow and have been shown to propagate a specific fibril structure[62,91]. In vitro kinetic assays with
366 SERF and MOAG-4 have shown that these peptides accelerate aggregation by acting on the nucleation
367 phase[65,68,92,93]. Recently, we have shown that SERF2 is equally capable to drive amyloid formation of
368 α-Syn and Aβ *in vitro* through a conserved, positively charged region[94]. Meanwhile, another study
369 has demonstrated that binding of the intrinsically disordered protein yeast SERF to α-Syn and Aβ
370 results in fuzzy complexes with heterogeneous structural conformations that are more

371 extended in nature[92]. For α-Syn, the disruption of intra-molecular electrostatic interactions by the
372 positively charged region of MOAG-4/SERF1 was found to expose an amyloid nucleation site[68,95].
373 Intra-molecular electrostatic interactions have also been proven to play a part in the dynamics and
374 structure of the Aβ monomer folding, which is at the basis of nucleus formation. In fact, several of the
375 familial AD mutations located within the Aβ sequence and reported not to affect the Aβ levels, appear
376 to exert their effects by modifying the intra-molecular interactions and monomer folding[96–99]. These
377 single amino acid modifications in the Aβ sequences also result in alterations in the aggregation
378 kinetics, fibril structure and aggregate toxicity in *in vitro* studies[100–102]. Moreover, patients and mouse
379 models with these mutations show differences in the localization of Aβ accumulation and deposition,
380 as well as differences in its structure, giving rise to specific disease phenotypes. For instance, while
381 some mutations result in increased Aβ deposition and altered plaque structure, other mutations at the
382 same location result in cerebral amyloid angiopathy with Aβ deposition in blood vessels rather than
383 the brain parenchyma or even an absence of extracellular Aβ deposition[35,99,111,112,103–110]. In addition,
384 some of these mutants showed increased intracellular Aβ accumulation which differed in structure-
385 specific staining characteristics[113–115]. The differences in Aβ pathology between these mutants seem to
386 display some similarities to the changes we observed between our AM and AM;*Serf2*$^{br-/-}$ mice.
387 Together with the *in vitro* findings about the mechanism of SERF2 interaction with aggregation-prone
388 proteins, this would appear to suggest modulation of intra-molecular interactions and altered
389 nucleation as the mechanism for SERF2's effect on aggregation and amyloid formation in our mice.
390 Interestingly, there is increasing evidence that qualitative, structural properties may be more related to
391 toxicity than the quantity of aggregates and deposits. Recent studies have provided increasing
392 evidence that structural polymorphs are associated with different clinical phenotypes in sporadic and
393 familial cases[59,61,62,85]. One recent study demonstrated that these structural conformations of distinct
394 disease phenotypes could also be detected by differences in the LCO spectra of the plaques and that
395 these spectral properties could, at least partially, be transmitted to a mouse model through seeding[85].
396 While the effect of familial mutations on the formation of distinct polymorphs has already been
397 explored by others[85,116–118], our study provides the first evidence of a single endogenous factor,
398 separate from Aβ and its production pathway, contributing to a structural shift of amyloid pathology in

399 a mammalian system. Further research will be needed to elucidate the exact structural changes at an
400 atomic level and if they affect toxicity and disease progression similarly to what was previously
401 observed in *C. elegans*. This will provide new insights into the structural properties and diversity of
402 disease-protein aggregation, contributing to a better understanding of the variability in disease
403 manifestation and open up previously unexplored avenues for therapeutic research.

404 Materials and methods

405 *Animals*

406 *Serf2* knockout mice were generated by introducing *loxP* sites in the *Serf2* gene on either side of exon
407 2, in accordance with the 'knockout-first' allele design as described by Skarnes and colleagues[119].
408 Full-body *Serf2* knockout mice were obtained by crossing these floxed mice with 129SV mice
409 expressing *Cre* under the *Hprt* promoter, resulting in the removal of exon 2 by *Cre*-mediated
410 recombination (Figure S1A). Subsequently, these mice with mixed background were backcrossed at
411 least 6 times to a C57Bl/6J background. Homozygous and heterozygous full-body *Serf2* knockout
412 mice were examined with their wild-type littermates at embryonic day 13.5, 15.5 and 17.5, as well as
413 at the day of birth (P0) and day of weaning (P22).

414 Heterozygous *Sox1-Cre* mice[76] were backcrossed at least 8 times to a C57BL/6J background. These
415 animals were also used as controls to differentiate between effects of *Cre* expression and Serf2
416 knockout. To generate the conditional *Serf2* knockout mice, the floxed mice were first crossed with
417 Tg(ACTFLPe)9205Dym (Jackson#003800) mice to flip the FRT site and remove the lacZ and neo
418 cassette. Subsequently, these mice were backcrossed at least 6 times to a C57BL/6J background.
419 Finally, the resulting homozygous *Serf2*$^{flox/flox}$ mice were crossed with the backcrossed *Sox1-Cre* mice,
420 to obtain the brain-specific *Serf2* knockout mice (Figure S3A). The conditional *Serf2* knockout mice
421 were crossed with the APPPS1-21 transgenic mice (APP (KM670/671NL)/PS1(L166P), Rottenburg,
422 Germany) [78]. A final cross between heterozygous APPPS1-21; *Serf2*$^{flox/flox}$ and heterozygous *Sox1-Cre*;
423 *Serf2*$^{flox/flox}$ resulted in four experimental groups of *Serf2*$^{flox/flox}$ mice: *Sox1-Cre*$^{-/-}$; APPPS1-21$^{-/-}$ (WT),

424 *Sox1-Cre*$^{+/-}$; APPPS1-21$^{-/-}$ (*Serf2*$^{br-/-}$), *Sox1-Cre*$^{-/-}$; APPPS1-21$^{+/-}$ (AM) and *Sox1-Cre*$^{+/-}$; APPPS1-21$^{+/-}$
425 (AM;*Serf2*$^{br-/-)}$ (Figure 2A). All experimental groups were tested at 1 month or 3 months of age.

426 All experiments were approved by the Institutional Animal Care and Use Committee of the University
427 of Groningen (Groningen, The Netherlands). All mice were maintained on a C57BL/6J background
428 and housed in a 12:12 hour light/dark cycle and the animals had ad libitum access to food and water.
429 Genotyping of embryos was performed using tail and yolk sac biopsies. Otherwise, ear biopsies were
430 used. DNA was purified using prepGEM® Tissue kit according to a protocol adapted from the
431 manufacturer (ZYGEPTI0500, ZyGEM, VWR International BV) and subjected to PCR using the
432 primers listed in Supplemental Table S5. Mice were terminated through CO_2-inhalation and cervical
433 dislocation for subsequent tissue collection.

434 *Embryo processing and histochemistry*

435 Embryos were fixed in 4 % formalin (Kinipath) for a minimum of 24 hours at room temperature. For
436 the pathological analysis, the embryos and their placenta were bisected longitudinally and embedded
437 in paraffin. Using the microm HM 340E (Thermo Scientific) 4 µm sections were cut for the
438 hematoxylin-eosin (HE) staining. The HE sections were incubated at 60 °C for 15 minutes. Next,
439 sections were deparaffinized and rehydrated in xylene (2x), 100 % alcohol (2x), 96 % alcohol, 70 %
440 alcohol and water. HE staining was performed by incubation with hematoxylin for 4 minutes, water
441 for 10 minutes, eosin for 1 minute and water for 10 seconds. After staining all sections were
442 dehydrated in 70 % alcohol, 96 % alcohol, 100 % alcohol (2x) and xylene (2x).

443 *Brain processing*

444 Upon termination, all brains were collected and weighed. From each experimental group three whole
445 brains were collected for HE staining according to the protocol described under embryo processing.
446 HE-stained sections were scanned with the TissueFAXs microscope using 20X objective. Images were
447 processed for nuclei counts using Histoquest software. The remaining brains were divided sagittally.
448 The left hemibrain was prepared for histochemistry and fixed in 4 % paraformaldehyde (PFA) for 48

449 hours at room temperature on a shaker. Next, the brains were placed in 30 % sucrose for
450 approximately 12 hours. Afterwards, the excess sucrose was removed and hemibrains were frozen in
451 molds with Tissue Tek O.C.T. compound (Sakura, The Netherlands) on dry ice. The right hemibrain
452 was snap frozen in liquid nitrogen and stored at -80°C. This tissue was homogenized using a liquid
453 nitrogen cooled mortar for subsequent protein and RNA analysis.

454 *Quantitative RT-PCR*

455 Total RNA was extracted from snap frozen tissue using TRIzol Reagent (Life Technologies) according
456 to the manufacturers' description. Total RNA quality and concentration were assessed using a
457 NanoDrop 2000 spectrophotometer (Thermo Scientific/Isogen Life Science). cDNA was made from
458 1,5 µg total RNA with a RevertAid H Minus First Strand cDNA Synthesis kit (Thermo Scientific)
459 using random hexamer primers. Quantitative real-time PCR was performed using a Roche LightCycler
460 480 Instrument II (Roche Diagnostics) with SYBR green dye (Bio-Rad Laboratories) to detect DNA
461 amplification. Relative transcript levels were quantitated using a standard curve of pooled cDNA
462 solutions. Expression levels were normalized to β-Actin or 18S mRNA levels. The primers for
463 Quantitative PCR used are listed in Supplemental Table S5.

464 *Western Blot analysis*

465 For SERF2 analysis tissues were homogenized in RIPA buffer (50 mM Tris pH 8, 150 mM NaCl,
466 5mM EDTA, 0.5 % SDS, 0.5 % SDO, 1 % NP-40) with protease inhibitor cocktail (Roche) and
467 incubated on ice for 1 hour, spun down at 13,300 rpm for 30 minutes at 4 °C and the supernatant was
468 collected. Protein measurements were performed using a BCA kit (Pierce) and 150 µg was loaded on a
469 10-20 % tris/tricine SDS-page gels (Bio-Rad Laboratories) and blotted onto 0,2 µm nitrocellulose
470 membrane (Bio-Rad Laboratories). Membranes were incubated overnight with SERF2 (1/1500,
471 Protein tech) or Actin (1/10 000, MP biomedicals) antibody. Next, the membranes were incubated
472 with anti-mouse or –rabbit secondary antibodies tagged with horseradish peroxidase (1/10 000, Bio-
473 Rad Laboratories) for one hour at room temperature and visualized by chemiluminescence (Amersham
474 ECL prime western blotting detection reagent, VWR).

475 *RNA sequencing*

476 RNA sequencing analysis was performed on three MEF cell lines from *Serf2*$^{-/-}$ mice and four *Serf2*$^{+/+}$
477 littermate controls. Total RNA was isolated from MEFs using the Qiagen RNeasy isolation kit.
478 Integrity of the RNA based on RIN scores as determined by a Bioanalyzer (Agilent). RNA-sequencing
479 libraries were prepared using TruSeq Stranded Total RNA with Ribo-Zero Human/Mouse/Rat (RS-
480 122-2201; Illumina, CA, USA) according to manufacturers' protocol. Pooled libraries were sequenced
481 on an Illumina HiSeq 2500 (single-end 50 bp). Reads were aligned to the mouse reference genome
482 (mm10) using a splicing-aware aligner (StarAligner). Aligned reads were normalized to fragments per
483 million (FPM), excluding low abundance genes (mean FPM>1 in at least two samples). The raw count
484 data were pre-processed using the programming language R (3.4.0) [R Core Team, 2016, available
485 online at: www.r-project.org], the program RStudio (1.0.143) [RStudio Team, 2016, available online
486 at: http://www.rstudio.com/] and the EdgeR package (3.18.0)(Robinson et al., 2010). Genes that
487 displayed FPM value >1 in at least two libraries were retained, resulting in a list of 12,808 genes for
488 differential analysis. Differentially expressed (DE) genes between the *Serf2*$^{+/+}$ and *Serf2*$^{-/-}$ MEFs were
489 identified using the EdgeR general linear model approach. After statistical correction for multiple
490 comparisons with the "false discovery rate" (FDR) method (FDR<0.05), a list of 738 DE genes was
491 obtained. DAVID (6.8) was used to perform functional annotation analyses on this gene list and to
492 identify significantly enriched gene ontology (GO) terms [using GOTERM_BP_DIRECT] [120,121]. The
493 connectivity between the enriched GO terms was further examined by determining the amount of
494 associated genes found (AGF) that were shared between two GO terms. The most significant
495 relationships (where a GO term shared > 25 % of the AGF) were mapped in a network using the
496 igraph package (1.0.1). The color of the edges reflects the major node, with the largest amount of
497 AGF, in each relationship. The weight of the edges was determined by the percentage of AGF shared
498 by the minor node in the relationship. We defined three clusters of GO-terms, where multiple minor
499 GO-terms connected to one or two central, major GO-terms . Minor GO-terms were always clustered
500 with the major GO-term with whom they shared the strongest connection. One GO term, positive

501 regulation of the apoptotic process, showed no direct relation with one of the major GO-terms and was
502 therefore assigned to the only cluster it had a significant connection with (Figure S2A-B).

503 *ELISA*

504 The ELISA experiments were performed as described previously[122]. Briefly, the frozen brain samples
505 were homogenized in tissue protein extraction reagent (Pierce) supplemented with complete protease
506 inhibitors (Roche), and centrifuged for 1 hour at 430 000 g at 4 °C. The supernatant was used for
507 ELISA. The $A\beta_{40}$ and $A\beta_{42}$ levels were determined by standard sandwich ELISAs using end-specific
508 antibodies (Janssen Pharmaceutical), and the monoclonal JRFcAβ_{40}/28 and JRFcAβ_{42}/26 antibodies as
509 the capture antibodies. Horseradish peroxidase conjugated JRFAβN/25 or JRFAβN/25 were used as
510 the detection antibodies for, respectively, human Aβ or murine Aβ. Samples were loaded in triplicate
511 for each ELISA. The ELISAs were performed in triplicate for the 3-month-old animals and in
512 duplicate for the 1-month-old animals.

513 *Brain immunohistochemistry*

514 To evaluate Aβ-related pathology, the brain was cut in 30 µm thick serial cryostat sections. A series of
515 sections was selected with 300 µm spacing between individual sections and blind-coded, 6 per mouse
516 for the 6E10 and Iba1 antibody and 3 per mouse for W02. Sections were fixed in 4 % PFA for 10
517 minutes, followed by 20 minutes antigen retrieval in citrate acid (pH 6.0) and 30 minutes in 1 % H_2O_2
518 in methanol. Next the sections were incubated for 1 hour in 10 % goat or donkey serum, depending on
519 the secondary antibody, and immunolabeled overnight with antibodies against Aβ, and Iba1
520 (Supplemental Table S6). The sections were washed and incubated with the complementary
521 biotinylated secondary antibody (1/500, Jackson Immunoresearch) for 2 hours. Next, sections were
522 incubated in ABC complex and reacted with diamino-benzidine (0.5 mg/ml H2O with 0.01 % H_2O_2).
523 The stained sections were scanned with the TissueFAXs microscope using 20X objective. All images
524 were analyzed using the Fiji platform of the ImageJ software[123]. For unbiased feature detection we
525 used a single automated script with optimized threshold method and parameters for the complete
526 image set of each staining method.

527 *Thioflavin-S Staining*

528 A 300 µm-spaced series of three blind-coded 30 µm sections were fixed in 4 % PFA for 10 min,
529 followed by incubation in 0.25 % potassium permanganate solution for 15 min, and a bleaching step
530 with 1 % potassium metabisulfite/1 % oxalic acid for 5 min, incubation with 0.02 % Thioflavin-S
531 solution in 50 % ethanol (Sigma T1892) for 8 minutes, rinsed with water between every step. Finally
532 the sections were incubated with 1 µl/ml DAPI. The sections were analyzed as described for the
533 immunostained sections. Stained sections were scanned with the TissueFAXs microscope using 20X
534 objective. Images were processed using Tissuequest software, selecting the cortex for automated
535 analyses.

536 *Luminescent conjugated oligothiophene (LCO) staining*

537 For the Luminescent conjugated oligothiophenes (LCO) stainings, two different LCO variants,
538 qFTAA (quadro-formyl thiophene acetic acid) and hFTAA (hepta-formyl thiophene acetic acid) were
539 used. Blind-coded 30 µm sections were double-stained with qFTAA and hFTAA (2.4 µM qFTAA and
540 0.77 µM hFTAA in PBS) similar to a previous description (Nyström et al., 2013). Sections were
541 incubated for 30 minutes in the dark at room temperature. Stainings were analyzed on the Zeiss LSM
542 510 META confocal microscope equipped with an argon 458 nm laser (Carl Zeiss MicroImaging
543 GmbH, Jena, Germany). An 40x objective (oil-immersion, 1.3 NA, Zeiss) was used for spectral
544 imaging of the Aβ deposits. Stacked images were acquired every 10 nm in the emission spectrum
545 between 470 to 695 nm. Locations were selected randomly from the plaque containing regions of the
546 temporal, frontal and occipital cortex. Images were analyzed using Fiji (Schindelin et al., 2012, 2015)
547 and standard computer algorithms to provide a reproducible, unbiased detection of the plaques. First,
548 the stacks of images across the different wavelengths of the spectrum were combined into one image
549 using the Z-projection sum. A threshold was applied to the resulting image using the "Triangle dark"
550 algorithm to automatically identify and delineate the plaques. Partial plaques on the edge of the images
551 and particles smaller than 25 μm^2 were excluded. These settings allowed us to detect over 98 % of all
552 the plaques in the images. The missed plaques were either too small or too low in intensity to be

553 accurately distinguished from the background. Incorrectly identified particles due to (lipofuscin) auto
554 fluorescence were readily identified based on their wavelength intensity profile and visual inspection
555 and were also excluded from the analysis. We identified between 17-25 plaques in each animal for the
556 spectral intensity measurements. The ratio of the intensity of emitted light at the blue-shifted portion
557 (502 nm) and red-shifted peak (588 nm) was used as a parameter for spectral distinction of different
558 Aβ deposits. These peaks of the spectra were selected to maximize the spectral distinction.

559 *Large-scale STEM (nanotomy)*

560 The scanning transmission electron microscopy (STEM) experiments were adapted from previously
561 described experiments (Kuipers et al., 2015). Briefly, paraffin embedded cortical sections of AM and
562 AM;*Serf2*$^{br-/-}$ were deparaffinized and postfixed with 1 % osmium tetroxide/1.5 % potassium
563 ferrocyanide in 0.1 M sodium cacodylate, dehydrated through ethanol and embedded in EPON (Serva)
564 using a tissue processor (Leica EM TP 709202). Ultrathin sections (80 nm) were cut using the Leica
565 uc7 ultramicrotome and collected on formvar coated cupper grids (electron microscopy sciences,
566 Hatfield, Pennsylvania). A large area scan using Scanning Transmission Detection was made using a
567 Zeiss supra55 SEM with Atlas. STEM detection with a four quadrant STEM detector was used in
568 inverted darkfield mode, at 28 kV with 30 µm aperture at 3.5 mm working distance. All images were
569 recorded at the same scan speed (cycle time 1.5 minute at 3072×2304 pixels). Contrast and brightness
570 were set based on a live histogram. High resolution large-scale STEM images at 2.5 nm pixel size
571 were generated with the external scan generator ATLAS (Fibics, Canada), individual tiles were
572 stitched in VE viewer (Fibics, Canada), exported as a html-file and uploaded to the website
573 www.nanotomy.org. Nanotomy datasets are open access available via the repository website
574 www.nanotomy.org/PW/temp02/EllenNollen.

575 ***[to be deleted] Upon acceptance of this work the website will be open access available, without***
576 ***password. Pending acceptance, the website can only be accessed by collaborators and reviewers***

577

578 *Cell culture*

579 Mouse embryonic fibroblasts (MEFs) were isolated from *Serf2*$^{+/+}$, *Serf2*$^{+/-}$ and *Serf2*$^{-/-}$ E13.5 embryos.
580 MEFs were cultured in T75 culture flasks (Greiner Bio-One, 658175), high–glucose Dulbecco's
581 modified Eagle's medium (Gibco), supplemented with 10% fetal bovine serum (Sigma 12133C), 1 %
582 penicillin/streptomycin (Gibco), non-essential amino acids (Gibco) and β-mercaptoethanol at 37°C, 5
583 % CO_2 and 3 % O_2. E13.5 embryos. Wild-type HEK293T and two independent clonal lines of
584 CRISPR *Serf2* KO mutant HEK 293T cells were cultured in Dulbecco's Modified Eagle Medium
585 (DMEM, Gibco; high glucose, pyruvate, 41966052), supplemented with 10 % Bovine Cow Serum
586 (BCS; Sigma 12133C) and 1 % Penicillin/Streptomycin (Gibco; 10 000 U/mL, 15140122), at 37 °C, 5
587 % CO_2. For passaging of cells, 0.05 % Trypsin-EDTA (1X), Phenol Red (Invitrogen; 25300-054) was
588 used. Regular mycoplasma tests were performed.

589 *Cell proliferation assay*

590 For the proliferation assay, 200 000 cells of each cell line were plated in triplicate in a standard 12-
591 well plate and incubated inside the IncuCyte Zoom Live-Cell Imaging System (Essen Bioscience) for
592 over 100 hours. The Incucyte system captured phase contrast images with a 10X magnification every 2
593 hours at nine distinct locations in each well to determine average confluency as a measure of cell
594 growth. The quantification was performed using the IncuCyte Zoom software. The growth experiment
595 was repeated three times. The confluency data of each experiment was normalized by min-max scaling
596 and the average of the three experiments was plotted (solid line) with the standard deviation (dashed
597 lines).

598 *Statistical analysis*

599 Unless specified otherwise, statistical analysis was performed using Graphpad v7.02. The exact
600 statistical test used for each comparison is specified in the main body of the text, together with the
601 resulting p-values. In the case of multiple comparisons, a post-hoc analysis with Bonferroni correction

was performed. Any corrected p-values derived from this post-hoc analysis are indicated in the text as p_{bon}.

Acknowledgments

All LCOs were kindly provided by K. Peter R. Nilsson, Linköping University, Sweden. Part of the work has been performed in the UMCG Microscopy and Imaging Center (UMIC), sponsored by ZonMW grant 91111.006 and NWO 40-00506-98-9021. We thank Ben Giepmans for advise on EM studies. This project was funded by a Meervoud Grant from NWO (836.09.001) (to E.A.A.N.), a European Research Council (ERC) starting grant (281622 PDControl) (to E.A.A.N.), the Alumni chapter Gooische Groningers facilitated by the Ubbo Emmius Fonds (to E.A.A.N), an Aspasia fellowship from NWO (015.014.005) (to E.A.A.N.), a Marie Curie Fellowship (to A.M.C.)

612 **References**

613 1. Glenner, G. G. & Wong, C. W. Alzheimer's disease: Initial report of the purification and
614 characterization of a novel cerebrovascular amyloid protein. *Biochem. Biophys. Res. Commun.*
615 (1984). doi:10.1016/S0006-291X(84)80190-4

616 2. Masters, C. L. *et al.* Amyloid plaque core protein in Alzheimer disease and Down syndrome.
617 *Proc. Natl. Acad. Sci. U. S. A.* **82**, 4245–4249 (1985).

618 3. Grundke-Iqbal, I. *et al.* Microtubule-associated protein tau. A component of Alzheimer paired
619 helical filaments. *J. Biol. Chem.* **261**, 6084–6089 (1986).

620 4. Grundke-Iqbal, I. *et al.* Abnormal phosphorylation of the microtubule-associated protein tau
621 (tau) in Alzheimer cytoskeletal pathology. *Proc. Natl. Acad. Sci. U. S. A.* **83**, 4913–4917
622 (1986).

623 5. Langley, C. H. & Charlesworth, B. *Nature © Macmillan Publishers Ltd 1997 expansion of*
624 *xenotransplantation*. (1997).

625 6. Scherzinger, E. *et al. Self-assembly of polyglutamine-containing huntingtin fragments into*
626 *amyloid-like fibrils: Implications for Huntington's disease pathology (huntingtinglutamine*
627 *repeataggregation). Medical Sciences Communicated by Max F. Perutz, Medical Research*
628 *Council* **96**, (1999).

629 7. Goate, A. *et al.* Segregation of a missense mutation in the amyloid precursor protein gene with
630 familial Alzheimer's disease. *Nature* **349**, 704–706 (1991).

631 8. Chartier-Harlin, M.-C. *et al.* Early-onset Alzheimer's disease caused by mutations at codon 717
632 of the β-amyloid precursor protein gene. *Nature* **353**, 844–846 (1991).

633 9. Citron, M. *et al.* Mutation of the β-amyloid precursor protein in familial Alzheimer's disease

634 increases β-protein production. *Nature* (1992). doi:10.1038/360672a0

635 10. Eckman, C. B. *et al.* A new pathogenic mutation in the APP gene (I716V) increases the relative
636 proportion of A beta 42(43). *Hum. Mol. Genet.* **6**, 2087–9 (1997).

637 11. Murrell, J. R., Hake, A. M., Quaid, K. A., Farlow, M. R. & Ghetti, B. Early-Onset Alzheimer
638 Disease Caused by a New Mutation (V717L) in the Amyloid Precursor Protein Gene. *Arch.*
639 *Neurol.* **57**, 885 (2000).

640 12. Kumar-Singh, S. *et al.* Nonfibrillar diffuse amyloid deposition due to a gamma(42)-secretase
641 site mutation points to an essential role for N-truncated A beta(42) in Alzheimer's disease.
642 *Hum. Mol. Genet.* **9**, 2589–98 (2000).

643 13. Cruts, M. *et al.* Novel APP mutation V715A associated with presenile Alzheimer's disease in a
644 German family. *J Neurol* **250**, 1374–1375 (2003).

645 14. Kumar-Singh, S. *et al.* Mean age-of-onset of familial Alzheimer disease caused by presenilin
646 mutations correlates with both increased Aβ42 and decreased Aβ40. *Hum. Mutat.* (2006).
647 doi:10.1002/humu.20336

648 15. Tomiyama, T. *et al.* A new amyloid β variant favoring oligomerization in Alzheimer's-type
649 dementia. *Ann. Neurol.* **63**, 377–387 (2008).

650 16. Schellenberg, G. *et al.* Genetic linkage evidence for a familial Alzheimer's disease locus on
651 chromosome 14. *Science (80-.).* **258**, 668–671 (1992).

652 17. Sherrington, R. *et al.* Cloning of a gene bearing missense mutations in early-onset familial
653 Alzheimer's disease. *Nature* **375**, 754–760 (1995).

654 18. Borchelt, D. R. *et al.* Familial Alzheimer's disease-linked presenilin I variants elevate aβ1-
655 42/1-40 ratio in vitro and in vivo. *Neuron* (1996). doi:10.1016/S0896-6273(00)80230-5

656 19. Lemere, C. A. *et al.* The E280A presenilin 1 Alzheimer mutation produces increased A beta 42
657 deposition and severe cerebellar pathology. *Nat. Med.* **2**, 1146–50 (1996).

658 20. Guerreiro, R. J. *et al.* Genetic screening of Alzheimer's disease genes in Iberian and African
659 samples yields novel mutations in presenilins and APP. *Neurobiol. Aging* **31**, 725–731 (2010).

660 21. Rogaev, E. I. *et al.* Familial Alzheimer's disease in kindreds with missense mutations in a gene
661 on chromosome 1 related to the Alzheimer's disease type 3 gene. *Nature* **376**, 775–778 (1995).

662 22. Citron, M. *et al.* Mutant presenilins of Alzheimer's disease increase production of 42-residue
663 amyloid beta-protein in both transfected cells and transgenic mice. *Nat. Med.* **3**, 67–72 (1997).

664 23. Müller, U., Winter, P., Bolender, C. & Nolte, D. Previously Unrecognized Missense Mutation
665 E126K of PSEN2 Segregates with Early Onset Alzheimer's Disease in a Family. *J. Alzheimer's*
666 *Dis.* **42**, 109–113 (2014).

667 24. Guerreiro, R. J. *et al.* Genetic screening of Alzheimer's disease genes in Iberian and African
668 samples yields novel mutations in presenilins and APP. *Neurobiol. Aging* **31**, 725–731 (2010).

669 25. Chartier-Harlin, M.-C. *et al.* Early-onset Alzheimer's disease caused by mutations at codon 717
670 of the β-amyloid precursor protein gene. *Nature* **353**, 844–846 (1991).

671 26. Citron, M. *et al.* Mutant presenilins of Alzheimer's disease increase production of 42-residue
672 amyloid beta-protein in both transfected cells and transgenic mice. *Nat. Med.* **3**, 67–72 (1997).

673 27. Eckman, C. B. *et al.* A new pathogenic mutation in the APP gene (I716V) increases the relative
674 proportion of A beta 42(43). *Hum. Mol. Genet.* **6**, 2087–9 (1997).

675 28. Kumar-Singh, S. *et al.* Nonfibrillar diffuse amyloid deposition due to a gamma(42)-secretase
676 site mutation points to an essential role for N-truncated A beta(42) in Alzheimer's disease.
677 *Hum. Mol. Genet.* **9**, 2589–98 (2000).

678 29. Lemere, C. A. *et al.* The E280A presenilin 1 Alzheimer mutation produces increased A beta 42
679 deposition and severe cerebellar pathology. *Nat. Med.* **2**, 1146–50 (1996).

680 30. Müller, U., Winter, P., Bolender, C. & Nolte, D. Previously Unrecognized Missense Mutation
681 E126K of PSEN2 Segregates with Early Onset Alzheimer's Disease in a Family. *J. Alzheimer's*
682 *Dis.* **42**, 109–113 (2014).

683 31. Murrell, J. R., Hake, A. M., Quaid, K. A., Farlow, M. R. & Ghetti, B. Early-Onset Alzheimer
684 Disease Caused by a New Mutation (V717L) in the Amyloid Precursor Protein Gene. *Arch.*
685 *Neurol.* **57**, 885 (2000).

686 32. Rogaev, E. I. *et al.* Familial Alzheimer's disease in kindreds with missense mutations in a gene
687 on chromosome 1 related to the Alzheimer's disease type 3 gene. *Nature* **376**, 775–778 (1995).

688 33. Schellenberg, G. *et al.* Genetic linkage evidence for a familial Alzheimer's disease locus on
689 chromosome 14. *Science (80-.).* **258**, 668–671 (1992).

690 34. Sherrington, R. *et al.* Cloning of a gene bearing missense mutations in early-onset familial
691 Alzheimer's disease. *Nature* **375**, 754–760 (1995).

692 35. Tomiyama, T. *et al.* A new amyloid β variant favoring oligomerization in Alzheimer's-type
693 dementia. *Ann. Neurol.* **63**, 377–387 (2008).

694 36. Haass, C. *et al.* The Swedish mutation causes early-onset Alzheimer's disease by beta-secretase
695 cleavage within the secretory pathway. *Nat. Med.* **1**, 1291–6 (1995).

696 37. Suzuki, N. *et al.* An increased percentage of long amyloid β protein secreted by familial
697 amyloid β protein precursor (βAPP717) mutants. *Science (80-.).* (1994).
698 doi:10.1126/science.8191290

699 38. Duff, K. *et al.* Increased amyloid-β42(43) in brains of mice expressing mutant presenilin 1.

700 *Nature* (1996). doi:10.1038/383710a0

701 39. Murayama, O. *et al.* Enhancement of amyloid β 42 secretion by 28 different presenilin 1
702 mutations of familial Alzheimer's disease. *Neurosci. Lett.* **265**, 61–63 (1999).

703 40. Nilsberth, C. *et al.* The 'Arctic' APP mutation (E693G) causes Alzheimer's disease by
704 enhanced Aβ protofibril formation. *Nat. Neurosci.* **4**, 887–893 (2001).

705 41. Miravalle, L. *et al.* Substitutions at Codon 22 of Alzheimer's A Peptide Induce Diverse
706 Conformational Changes and Apoptotic Effects in Human Cerebral Endothelial Cells*. (2000).
707 doi:10.1074/jbc.M003154200

708 42. Ni, C.-L., Shi, H.-P., Yu, H.-M., Chang, Y.-C. & Chen, Y.-R. Folding stability of amyloid-β 40
709 monomer is an important determinant of the nucleation kinetics in fibrillization. *FASEB J.* **25**,
710 1390–1401 (2011).

711 43. Conway, K. A., Harper, J. D. & Lansbury, P. T. Accelerated in vitro fibril formation by a
712 mutant α-synuclein linked to early-onset Parkinson disease. *Nat. Med.* (1998).
713 doi:10.1038/3311

714 44. Narhi, L. *et al.* Both Familial Parkinson's Disease Mutations Accelerate α-Synuclein
715 Aggregation. *J. Biol. Chem.* **274**, 9843–9846 (1999).

716 45. Conway, K. A. *et al.* Acceleration of oligomerization, not fibrillization, is a shared property of
717 both α-synuclein mutations linked to early-onset Parkinson's disease: Implications for
718 pathogenesis and therapy. *Proc. Natl. Acad. Sci. U. S. A.* (2000). doi:10.1073/pnas.97.2.571

719 46. Ghosh, D. *et al.* The Parkinson's Disease-Associated H50Q Mutation Accelerates α-Synuclein
720 Aggregation *in Vitro*. *Biochemistry* **52**, 6925–6927 (2013).

721 47. Ghosh, D. *et al.* The Newly Discovered Parkinson's Disease Associated Finnish Mutation

722 (A53E) Attenuates α-Synuclein Aggregation and Membrane Binding. *Biochemistry* **53**, 6419–
723 6421 (2014).

724 48. Choi, W. *et al.* Mutation E46K increases phospholipid binding and assembly into filaments of
725 human α-synuclein. *FEBS Lett.* **576**, 363–368 (2004).

726 49. Cooper, J. K. *et al.* Truncated N-terminal fragments of huntingtin with expanded glutamine
727 repeats form nuclear and cytoplasmic aggregates in cell culture. *Hum. Mol. Genet.* (1998).
728 doi:10.1093/hmg/7.5.783

729 50. Nekooki-Machida, Y. *et al.* Distinct conformations of in vitro and in vivo amyloids of
730 huntingtin-exon1 show different cytotoxicity. *Proc. Natl. Acad. Sci. U. S. A.* **106**, 9679–84
731 (2009).

732 51. Sun, C.-S. *et al.* Conformational switch of polyglutamine-expanded huntingtin into benign
733 aggregates leads to neuroprotective effect. *Sci. Rep.* **5**, 14992 (2015).

734 52. Cohen, M. L. *et al.* Rapidly progressive Alzheimer's disease features distinct structures of
735 amyloid-β. *Brain* **138**, 1009–1022 (2015).

736 53. Qiang, W., Yau, W.-M., Lu, J.-X., Collinge, J. & Tycko, R. Structural variation in amyloid-β
737 fibrils from Alzheimer's disease clinical subtypes. *Nature* **541**, 217–221 (2017).

738 54. Bousset, L. *et al.* Structural and functional characterization of two alpha-synuclein strains. *Nat.*
739 *Commun.* **4**, 2575 (2013).

740 55. Heise, H. *et al.* Solid-State NMR Reveals Structural Differences between Fibrils of Wild-Type
741 and Disease-Related A53T Mutant α-Synuclein. *J. Mol. Biol.* **380**, 444–450 (2008).

742 56. Li, B. *et al.* Cryo-EM of full-length α-synuclein reveals fibril polymorphs with a common
743 structural kernel. *Nat. Commun.* **9**, 3609 (2018).

744 57. Guerrero-Ferreira, R. *et al.* Two new polymorphic structures of alpha-synuclein solved by
745 cryo-electron microscopy. *bioRxiv* 654582 (2019). doi:10.1101/654582

746 58. Gath, J. *et al.* Unlike Twins: An NMR Comparison of Two α-Synuclein Polymorphs Featuring
747 Different Toxicity. *PLoS One* **9**, e90659 (2014).

748 59. Lu, J. X. *et al.* Molecular structure of β-amyloid fibrils in alzheimer's disease brain tissue. *Cell*
749 (2013). doi:10.1016/j.cell.2013.08.035

750 60. Rasmussen, J. *et al.* Amyloid polymorphisms constitute distinct clouds of conformational
751 variants in different etiological subtypes of Alzheimer's disease. *Proc. Natl. Acad. Sci.* **114**,
752 13018–13023 (2017).

753 61. Cohen, M. L. *et al.* Rapidly progressive Alzheimer's disease features distinct structures of
754 amyloid-β. *Brain* **138**, 1009–1022 (2015).

755 62. Qiang, W., Yau, W.-M., Lu, J.-X., Collinge, J. & Tycko, R. Structural variation in amyloid-β
756 fibrils from Alzheimer's disease clinical subtypes. *Nature* **541**, 217–221 (2017).

757 63. van Ham, T. J. *et al.* Identification of MOAG-4/SERF as a regulator of age-related
758 proteotoxicity. *Cell* **142**, 601–612 (2010).

759 64. van Ham, T. J. *et al.* Identification of MOAG-4/SERF as a regulator of age-related
760 proteotoxicity. *Cell* **142**, 601–612 (2010).

761 65. Falsone, S. F. *et al.* SERF Protein Is a Direct Modifier of Amyloid Fiber Assembly. *Cell Rep.*
762 **2**, 358–371 (2012).

763 66. Yoshimura, Y. *et al.* MOAG-4 promotes the aggregation of α-synuclein by competing with
764 self-protective electrostatic interactions. *J. Biol. Chem.* **292**, 8269–8278 (2017).

765 67. Merle, D. A. *et al.* Increased Aggregation Tendency of Alpha-Synuclein in a Fully Disordered
766 Protein Complex. *J. Mol. Biol.* **431**, 2581–2598 (2019).

767 68. Yoshimura, Y. *et al.* MOAG-4 promotes the aggregation of α-synuclein by competing with
768 self-protective electrostatic interactions. *J. Biol. Chem.* **292**, 8269–8278 (2017).

769 69. Kaufman, M. H. *The Atlas of Mouse Development*. (Elsevier Science, 1992).

770 70. Kaufman, M. H. & Bard, J. B. L. *The Anatomical Basis of Mouse Development*. (Elsevier
771 Science, 1999).

772 71. Ward, J. M., Elmore, S. A. & Foley, J. F. Pathology Methods for the Evaluation of Embryonic
773 and Perinatal Developmental Defects and Lethality in Genetically Engineered Mice. *Vet.*
774 *Pathol.* **49**, 71–84 (2012).

775 72. Ciemerych, M. A. & Sicinski, P. Cell cycle in mouse development. *Oncogene* (2005).
776 doi:10.1038/sj.onc.1208608

777 73. Takashima, Y. *et al.* Neuroepithelial Cells Supply an Initial Transient Wave of MSC
778 Differentiation. *Cell* **129**, 1377–1388 (2007).

779 74. Pevny, L. H., Sockanathan, S., Placzek, M. & Lovell-Badge, R. A role for SOX1 in neural
780 determination. *Development* (1998).

781 75. Wood, H. B. & Episkopou, V. Comparative expression of the mouse Sox1, Sox2 and Sox3
782 genes from pre-gastrulation to early somite stages. *Mech. Dev.* (1999). doi:10.1016/S0925-
783 4773(99)00116-1

784 76. Takashima, Y. *et al.* Neuroepithelial Cells Supply an Initial Transient Wave of MSC
785 Differentiation. *Cell* **129**, 1377–1388 (2007).

786 77. Radde, R. *et al.* Abeta42-driven cerebral amyloidosis in transgenic mice reveals early and
787 robust pathology. *EMBO Rep.* **7**, 940–6 (2006).

788 78. Radde, R. *et al.* Abeta42-driven cerebral amyloidosis in transgenic mice reveals early and
789 robust pathology. *EMBO Rep.* **7**, 940–6 (2006).

790 79. Klingstedt, T. *et al.* Synthesis of a library of oligothiophenes and their utilization as fluorescent
791 ligands for spectral assignment of protein aggregates. *Org. Biomol. Chem.* **9**, 8356–70 (2011).

792 80. Psonka-Antonczyk, K. M. *et al.* Nanoscale Structure and Spectroscopic Probing of Aβ1-40
793 Fibril Bundle Formation. *Front. Chem.* (2016). doi:10.3389/fchem.2016.00044

794 81. Nyström, S. *et al.* Evidence for Age-Dependent in Vivo Conformational Rearrangement within
795 Aβ Amyloid Deposits. *ACS Chem. Biol.* **8**, 1128–1133 (2013).

796 82. Klingstedt, T. *et al.* Synthesis of a library of oligothiophenes and their utilization as fluorescent
797 ligands for spectral assignment of protein aggregates. *Org. Biomol. Chem.* **9**, 8356–70 (2011).

798 83. Nyström, S. *et al.* Evidence for Age-Dependent in Vivo Conformational Rearrangement within
799 Aβ Amyloid Deposits. *ACS Chem. Biol.* **8**, 1128–1133 (2013).

800 84. Lord, A. *et al.* Observations in APP bitransgenic mice suggest that diffuse and compact plaques
801 form via independent processes in Alzheimer's disease. *Am. J. Pathol.* **178**, 2286–2298 (2011).

802 85. Rasmussen, J. *et al.* Amyloid polymorphisms constitute distinct clouds of conformational
803 variants in different etiological subtypes of Alzheimer's disease. *Proc. Natl. Acad. Sci.* **114**,
804 13018–13023 (2017).

805 86. Meyer, N. H. *et al.* Structural fuzziness of the RNA-organizing protein SERF1a determines a
806 toxic gain-of-interaction. *bioRxiv* 713511 (2019). doi:10.1101/713511

807 87. Murray, S. A. *et al.* Mouse Gestation Length Is Genetically Determined. *PLoS One* **5**, e12418
808 (2010).

809 88. Meyer, N. H. *et al.* Structural fuzziness of the RNA-organizing protein SERF1a determines a
810 toxic gain-of-interaction. *bioRxiv* 713511 (2019). doi:10.1101/713511

811 89. Visintin, R. & Amon, A. The nucleolus: the magician's hat for cell cycle tricks. *Curr. Opin.*
812 *Cell Biol.* **12**, 372–377 (2000).

813 90. Leung, A. K. L. *et al.* Quantitative kinetic analysis of nucleolar breakdown and reassembly
814 during mitosis in live human cells. *J. Cell Biol.* **166**, 787–800 (2004).

815 91. Petkova, A. T. *et al.* Self-propagating, molecular-level polymorphism in Alzheimer's β-
816 amyloid fibrils. *Science (80-.).* (2005). doi:10.1126/science.1105850

817 92. Meinen, B. A., Gadkari, V. V., Stull, F., Ruotolo, B. T. & Bardwell, J. C. A. SERF engages in
818 a fuzzy complex that accelerates primary nucleation of amyloid proteins. *Proc. Natl. Acad. Sci.*
819 (2019). doi:10.1073/pnas.1913316116

820 93. Merle, D. A. *et al.* Increased Aggregation Tendency of Alpha-Synuclein in a Fully Disordered
821 Protein Complex. *J. Mol. Biol.* **431**, 2581–2598 (2019).

822 94. Pras, A. *et al.* The cellular modifier MOAG-4/SERF drives amyloid formation through charge
823 complementation. *bioRxiv* 2020.12.09.417709 (2020). doi:10.1101/2020.12.09.417709

824 95. Merle, D. A. *et al.* Increased Aggregation Tendency of Alpha-Synuclein in a Fully Disordered
825 Protein Complex. *J. Mol. Biol.* (2019). doi:10.1016/j.jmb.2019.04.031

826 96. Grant, M. A. *et al. Familial Alzheimer's disease mutations alter the stability of the amyloid-*
827 *protein monomer folding nucleus*. **104**, (2007).

828 97. Lazo, N. D., Grant, M. A., Condron, M. C., Rigby, A. C. & Teplow, D. B. On the nucleation of
829 amyloid β-protein monomer folding. *Protein Sci.* **14**, 1581–1596 (2009).

830 98. Elkins, M. R. *et al.* Structural Polymorphism of Alzheimer's β-Amyloid Fibrils as Controlled
831 by an E22 Switch: A Solid-State NMR Study. (2016). doi:10.1021/jacs.6b03715

832 99. Ni, C.-L., Shi, H.-P., Yu, H.-M., Chang, Y.-C. & Chen, Y.-R. Folding stability of amyloid-β 40
833 monomer is an important determinant of the nucleation kinetics in fibrillization. *FASEB J.* **25**,
834 1390–1401 (2011).

835 100. Ovchinnikova, O. Y., Finder, V. H., Vodopivec, I., Nitsch, R. M. & Glockshuber, R. The
836 Osaka FAD Mutation E22Δ Leads to the Formation of a Previously Unknown Type of
837 Amyloid β Fibrils and Modulates Aβ Neurotoxicity. *J. Mol. Biol.* **408**, 780–791 (2011).

838 101. Van Nostrand, W. E., Melchor, J. P., Cho, H. S., Greenberg, S. M. & Rebeck, G. W.
839 Pathogenic effects of D23N Iowa mutant amyloid beta -protein. *J. Biol. Chem.* **276**, 32860–6
840 (2001).

841 102. Miravalle, L. *et al.* Substitutions at Codon 22 of Alzheimer's A Peptide Induce Diverse
842 Conformational Changes and Apoptotic Effects in Human Cerebral Endothelial Cells*. (2000).
843 doi:10.1074/jbc.M003154200

844 103. Inayathullah, M. & Teplow, D. B. Structural dynamics of the Δe22 (Osaka) familial
845 Alzheimer's disease-linked amyloid β-protein. *Amyloid* **18**, 98–107 (2011).

846 104. Bugiani, O. *et al.* Hereditary Cerebral Hemorrhage With Amyloidosis Associated With the
847 E693K Mutation of APP. *Arch. Neurol.* **67**, 987–995 (2010).

848 105. Grabowski, T. J., Cho, H. S., Vonsattel, J. P. G., Rebeck, G. W. & Greenberg, S. M. Novel
849 amyloid precursor protein mutation in an Iowa family with dementia and severe cerebral
850 amyloid angiopathy. *Ann. Neurol.* **49**, 697–705 (2001).

851 106. Philipson, O. *et al.* A highly insoluble state of Aβ similar to that of Alzheimer's disease brain is
852 found in Arctic APP transgenic mice. *Neurobiol. Aging* **30**, 1393–1405 (2009).

853 107. Shimada, H. *et al.* Clinical course of patients with familial early-onset Alzheimer's disease
854 potentially lacking senile plaques bearing the E693Δ mutation in amyloid precursor protein.
855 *Dement. Geriatr. Cogn. Disord.* **32**, 45–54 (2011).

856 108. Tomiyama, T. *et al.* A Mouse Model of Amyloid β Oligomers: Their Contribution to Synaptic
857 Alteration, Abnormal Tau Phosphorylation, Glial Activation, and Neuronal Loss In Vivo. *J.*
858 *Neurosci.* **30**, 4845–4856 (2010).

859 109. Grant, M. A. *et al. Familial Alzheimer's disease mutations alter the stability of the amyloid-*
860 *protein monomer folding nucleus*. **104**, (2007).

861 110. Nilsberth, C. *et al.* The 'Arctic' APP mutation (E693G) causes Alzheimer's disease by
862 enhanced Aβ protofibril formation. *Nat. Neurosci.* **4**, 887–893 (2001).

863 111. Lord, A. *et al.* Observations in APP bitransgenic mice suggest that diffuse and compact plaques
864 form via independent processes in Alzheimer's disease. *Am. J. Pathol.* **178**, 2286–2298 (2011).

865 112. Van Nostrand, W. E., Melchor, J. P., Cho, H. S., Greenberg, S. M. & Rebeck, G. W.
866 Pathogenic effects of D23N Iowa mutant amyloid beta -protein. *J. Biol. Chem.* **276**, 32860–6
867 (2001).

868 113. Lord, A. *et al.* The Arctic Alzheimer mutation facilitates early intraneuronal Aβ aggregation
869 and senile plaque formation in transgenic mice. *Neurobiol. Aging* **27**, 67–77 (2006).

870 114. Kulic, L. *et al.* Early accumulation of intracellular fibrillar oligomers and late congophilic
871 amyloid angiopathy in mice expressing the Osaka intra-Aβ APP mutation. *Transl. Psychiatry*
872 **2**, e183–e183 (2012).

873 115. Tomiyama, T. *et al.* A Mouse Model of Amyloid β Oligomers: Their Contribution to Synaptic
874 Alteration, Abnormal Tau Phosphorylation, Glial Activation, and Neuronal Loss In Vivo. *J.*
875 *Neurosci.* **30**, 4845–4856 (2010).

876 116. Philipson, O. *et al.* The Arctic amyloid-β precursor protein (AβPP) mutation results in distinct
877 plaques and accumulation of N- and C-truncated Aβ. *Neurobiol. Aging* **33**, 1010.e1-1010.e13
878 (2012).

879 117. Lord, A. *et al.* The Arctic Alzheimer mutation facilitates early intraneuronal Aβ aggregation
880 and senile plaque formation in transgenic mice. *Neurobiol. Aging* **27**, 67–77 (2006).

881 118. Kulic, L. *et al.* Early accumulation of intracellular fibrillar oligomers and late congophilic
882 amyloid angiopathy in mice expressing the Osaka intra-Aβ APP mutation. *Transl. Psychiatry*
883 **2**, e183–e183 (2012).

884 119. Skarnes, W. C. *et al.* A conditional knockout resource for the genome-wide study of mouse
885 gene function. *Nature* **474**, 337–342 (2011).

886 120. Huang, D. W., Sherman, B. T. & Lempicki, R. A. Systematic and integrative analysis of large
887 gene lists using DAVID bioinformatics resources. *Nat. Protoc.* **4**, 44–57 (2009).

888 121. Huang, D. W., Sherman, B. T. & Lempicki, R. A. Bioinformatics enrichment tools: paths
889 toward the comprehensive functional analysis of large gene lists. *Nucleic Acids Res.* **37**, 1–13
890 (2009).

891 122. Huang, Y. *et al.* Loss of GPR3 reduces the amyloid plaque burden and improves memory in
892 Alzheimer's disease mouse models. *Sci. Transl. Med.* **7**, 309ra164 (2015).

893 123. Schindelin, J. *et al.* Fiji: an open-source platform for biological-image analysis. *Nat. Methods*
894 **9**, 676–682 (2012).

895 **Figure legends**

896 **Figure 1. Full-body *Serf2*$^{-/-}$ mice display a developmental delay and perinatal lethality. (A)**
897 Schematic overview of the crossing scheme with full-body *Serf2*$^{+/-}$ mice and the resulting genotypic
898 composition of the offspring at embryonic and postnatal stage. **(B)** Absolute animal counts for the
899 three genotypes in the offspring at various days of embryonic development(E13.5, E15.5 and E17.5),
900 at birth (P0) and at time of weaning (P22). **(C)** Real time RT-PCR analyses of *Serf1* and *Serf2* RNA
901 levels in E13.5 heads normalized to housekeeping gene beta-actin (n=4/group, mean±SD, One-way
902 ANOVA for each gene, Bonferroni corrected post-hoc comparison between genotypes ***p<0.001).
903 **(D)** Western blot of SERF2 and actin in *Serf2*$^{+/+}$, *Serf2*$^{+/-}$, *Serf2*$^{-/-}$embryos at E13.5 (black arrow
904 indicates SERF2 band). **(E)** Length measurements of *Serf2*$^{+/+}$, *Serf2*$^{+/-}$, *Serf2*$^{-/-}$ embryos at E15.5, E17.5
905 and P0 (black line = mean, Two-way ANOVA with factors age and genotype, Bonferroni corrected
906 post-hoc comparison for *Serf2*$^{+/-}$ and *Serf2*$^{-/-}$ compared to *Serf2*$^{-/-}$ *p<0.05; ***p<0.001). **(F)**
907 Hematoxylin and eosin stained lung tissue from *Serf2*$^{+/+}$ and *Serf2*$^{-/-}$ pups at P0 (top: *Serf2*$^{-/-}$, bottom:
908 *Serf2*$^{+/+}$, scale bar=500µm, rectangle =5x magnification in right picture, **(G)** Quantification of the
909 saccolar space in lung tissue from *Serf2*$^{+/+}$ and *Serf2*$^{-/-}$ pups at P0 (black line = mean, t-test **p<0.01).
910 For all mouse data panels: *Serf2*$^{+/+}$= black, *Serf2*$^{+/-}$ = dark grey, *Serf2*$^{-/-}$ = light grey.

911 **Figure 2. Crossing a conditional *Serf2* KO with an AM background does not affect the overall**
912 **levels of APP and Aβ. (A)** Schematic overview of the cross between brain-specific *Serf2* KO mice
913 and the amyloid model resulting in four experimental groups: WT, *Serf2*$^{br-/-}$, AM and AM;*Serf2*$^{br-/-}$.
914 **(B)** Timeline for the Aβ pathology in the amyloid model and the selected time points for this study.
915 **(C)** Real time RT-PCR analyses of *Serf2* RNA levels in the brain tissue of all experimental groups at 1
916 and 3 months of age normalized to housekeeping gene beta-actin (n=6/group, mean±SD, Two-way
917 ANOVA with factors age and genotype, Bonferroni corrected post-hoc for individual groups
918 compared to WT). **(D)** Western blot of SERF2 and actin in brain tissue of all experimental groups at 1
919 and 3 months of age. **(E)** Brain weight of all experimental groups at 1 and 3 months of age (black line
920 = mean, Two-way ANOVA with factors age and genotype, Bonferroni corrected post-hoc for

921 individual groups compared to WT). **(F)** Brain weight of unfloxed control groups at 3 months of age
922 (black line = mean, One-way ANOVA, Bonferroni corrected post-hoc for individual groups compared
923 to WT). **(G)** Number of cortical nuclei per mm^2 in hematoxylin and eosin stained brain tissue of all
924 experimental groups at 3 months of age. (n=3/group, mean±SD, Kruskal-Wallis p=0.5566). **(H)** Real
925 time RT-PCR analyses of APP RNA levels in the brain tissue of AM and AM;*Serf2*$^{br-/-}$ mice at 1 and 3
926 months of age normalized to housekeeping gene beta-actin (n=6/group, mean±SD, t-test between
927 genotypes at both ages not significant). **(I)** Western blot of APP and beta-actin in brain tissue of AM
928 and AM;*Serf2*$^{br-/-}$ mice at 3 months of age versus 1-month-old non-AM controls. **(J)** Quantification of
929 total APP protein levels in brains of AM and AM;*Serf2*$^{br-/-}$ mice at 1 and 3 months of age normalized
930 to beta-actin levels. (black line = mean, t-test between genotypes at both ages not significant). **(K)**
931 $A\beta_{40}$ and **(L)** $A\beta_{42}$ levels in brain lysate from AM and AM;*Serf2*$^{br-/-}$ mice at 1 and 3 months of age as
932 determined by ELISA normalized to total protein content. (black line = mean, t-test between
933 genotypes at both ages not significant). **(M)** Correlation plot depicting the relationship between $A\beta_{40}$
934 and $A\beta_{42}$ levels in AM (black) and AM;*Serf2*$^{br-/-}$ (grey) mice at 3 months of age (detailed statistics in
935 Supplemental Table 3). In panels A-L: WT = black, *Serf2*$^{br-/-}$ = light grey , AM = dark grey and
936 AM;*Serf2*$^{br-/-}$ = white; ***p<0.001; **p<0.01.

937 **Figure 3. Brain-specific *Serf2* KO display increased Aβ deposition and amyloid .(A)** Detailed light
938 microscope images of the 6E10-stained cortical region marked on the sagittal section in Supplemental
939 Figure 5 from 3-month-old AM and AM;*Serf2*$^{br-/-}$ mice (scale bar = 100μm). **(B)** Quantification of the
940 Aβ deposits in the region of interest (ROI) of 6E10 immunostained sagittal brain sections from 1- and
941 3-month-old AM and AM;*Serf2*$^{br-/-}$ mice (black line = mean, One-way ANOVA between genotypes at
942 both ages, Bonferroni corrected post-hoc between AM and AM;*Serf2*$^{br-/-}$ not significant). **(C)**
943 Correlation plot depicting the relationship between $A\beta_{40}$ levels and 6E10 plaque density in AM (black)
944 and AM;*Serf2*$^{br-/-}$ (grey) mice at 3 months of age. **(D)** Correlation plot depicting the relationship
945 between $A\beta_{42}$ levels and 6E10 plaque density in AM (black) and AM;*Serf2*$^{br-/-}$ (grey) mice at 3 months
946 of age. **(E)** Quantification of the Aβ deposits in the ROI of W0-2 immunostained sagittal brain
947 sections from 1- and 3-month-old AM and AM;*Serf2*$^{br-/-}$ mice (black line = mean, One-way ANOVA

948 between genotypes at both ages, Bonferroni corrected post-hoc between AM and AM;*Serf2*$^{br-/-}$ not
949 significant). **(F)** Correlation plot depicting the relationship between 6E10 deposits and W0-2 deposits
950 in AM (black) and AM;*Serf2*$^{br-/-}$ (grey) mice at 3 months of age. **(G)** Quantification of the plaque
951 density in the ROI of Thioflavin-S stained sagittal brain sections from 1- and 3-month-old AM and
952 AM;*Serf2*$^{br-/-}$ mice (black line = mean, One-way ANOVA between genotypes at both ages, Bonferroni
953 corrected post-hoc between AM and AM;*Serf2*$^{br-/-}$ not significant). **(H)** Correlation plot depicting the
954 relationship between Aβ_{40} levels and ThS plaque density in AM (black) and AM;*Serf2*$^{br-/-}$ (grey) mice
955 at 3 months of age. **(I)** Correlation plot depicting the relationship between Aβ_{42} levels and ThS plaque
956 density in AM (black) and AM;*Serf2*$^{br-/-}$ (grey) mice at 3 months of age. **(I)** Correlation plot depicting
957 the relationship between 6E10 deposits and ThS plaques in AM (black) and AM;*Serf2*$^{br-/-}$ (grey) mice
958 at 3 months of age. In all panels ROI = cortical and hippocampal area; In panels B,E and G: WT =
959 black, *Serf2*$^{br-/-}$ = light grey , AM = dark grey and AM;*Serf2*$^{br-/-}$ = white; for correlation plots: detailed
960 statistics in Supplemental Table 3; ***p<0.001; **p<0.01; *p <0.05.

961 **Figure 4. Brain-specific *Serf2* KO alters the structural composition of amyloid plaques. (A)**
962 Graph showing the theoretical LCO dye emission spectra for qFTAA, which binds mature Aβ fibrils
963 (blue), and hFTAA, which binds both mature fibrils and prefibrillar Aβ species (red). **(B)** Frequency
964 distribution of the ratio in fluorescence intensity at 502 nm and 588 nm for all amyloid plaques
965 identified by confocal microscopy in AM (blue) and AM;*Serf2*$^{br-/-}$ (red) mice at 3 months of age. Three
966 peak frequency categories were identified: low IR(red), medium IR (green) and high IR (blue) (n=6
967 mice/genotype). **(C)** Dot plot representing the intensity ratio of all amyloid plaques identified by
968 confocal microscopy for AM and AM;*Serf2*$^{br-/-}$ mice at 3 months of age (colors represent the IR
969 categories defined in panel B, black circles correspond to the plaques depicted in panel E, black line =
970 mean, t-test ***p<0.001) (n=6 mice/genotype). **(D)** Correlation plot depicting the relationship between
971 6E10 plaque density in the ROI and the LCO average intensity ratio in AM (black) and AM;*Serf2*$^{br-/-}$
972 (grey) mice at 3 months of age (ROI = cortical and hippocampal area, detailed statistics in
973 Supplemental Table 3). **(E)** Spectral confocal microscopy images of amyloid plaques in AM and
974 AM;*Serf2*$^{br-/-}$ mice at 3 months of age of double stained with qFTAA and hFTAA (top= fluorescence

975 at 502 nm, middle= fluorescence at 588 nm, bottom=merged image of 502 nm and 588 nm
976 fluorescence, scale bar = 5 µm). **(F)** Scanning transmission electron microscopy pictures of amyloid
977 plaques in the cortex of AM and AM;*Serf2*$^{br-/-}$ mice at 3 months of age (top scale bar 5µm, rectangle =
978 zoomed region in bottom picture, bottom scale bar = 1µm). High-resolution EM images are available
979 via http://www.nanotomy.org.

Figure 1

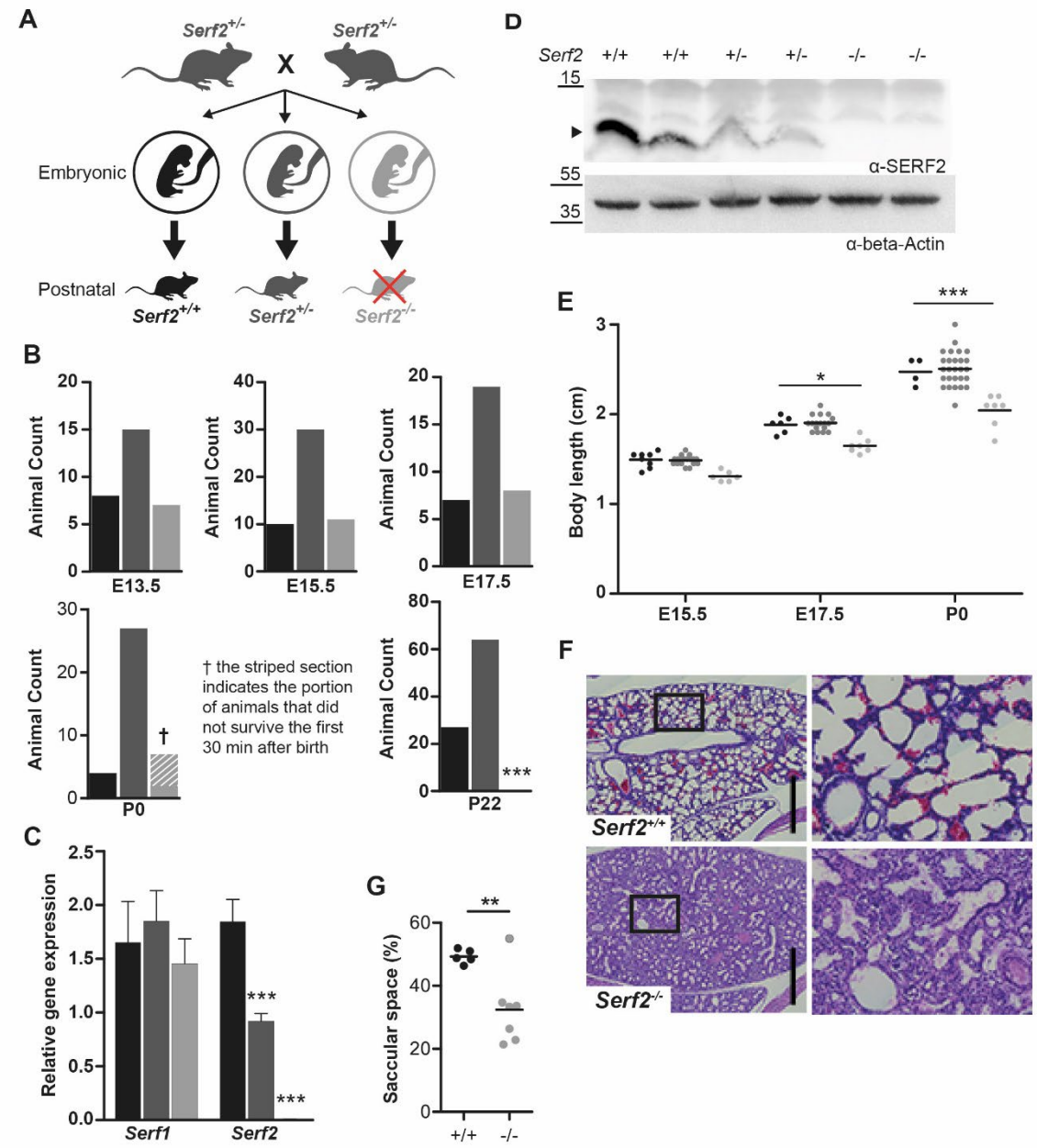
A
Serf2+/-
X
Serf2+/-
Embryonic
Postnatal
Serf2+/+
Serf2+/-
Serf2-/-
B
Animal Count
E13.5
E15.5
E17.5
P0
P22
† the striped section indicates the portion of animals that did not survive the first 30 min after birth
C
Relative gene expression
Serf1
Serf2
D
Serf2 +/+ +/+ +/- +/- -/- -/-
15
55
35
α-SERF2
α-beta-Actin
E
Body length (cm)
E15.5
E17.5
P0
F
Serf2+/+
Serf2-/-
G
Saccular space (%)
+/+
-/-

Figure 2

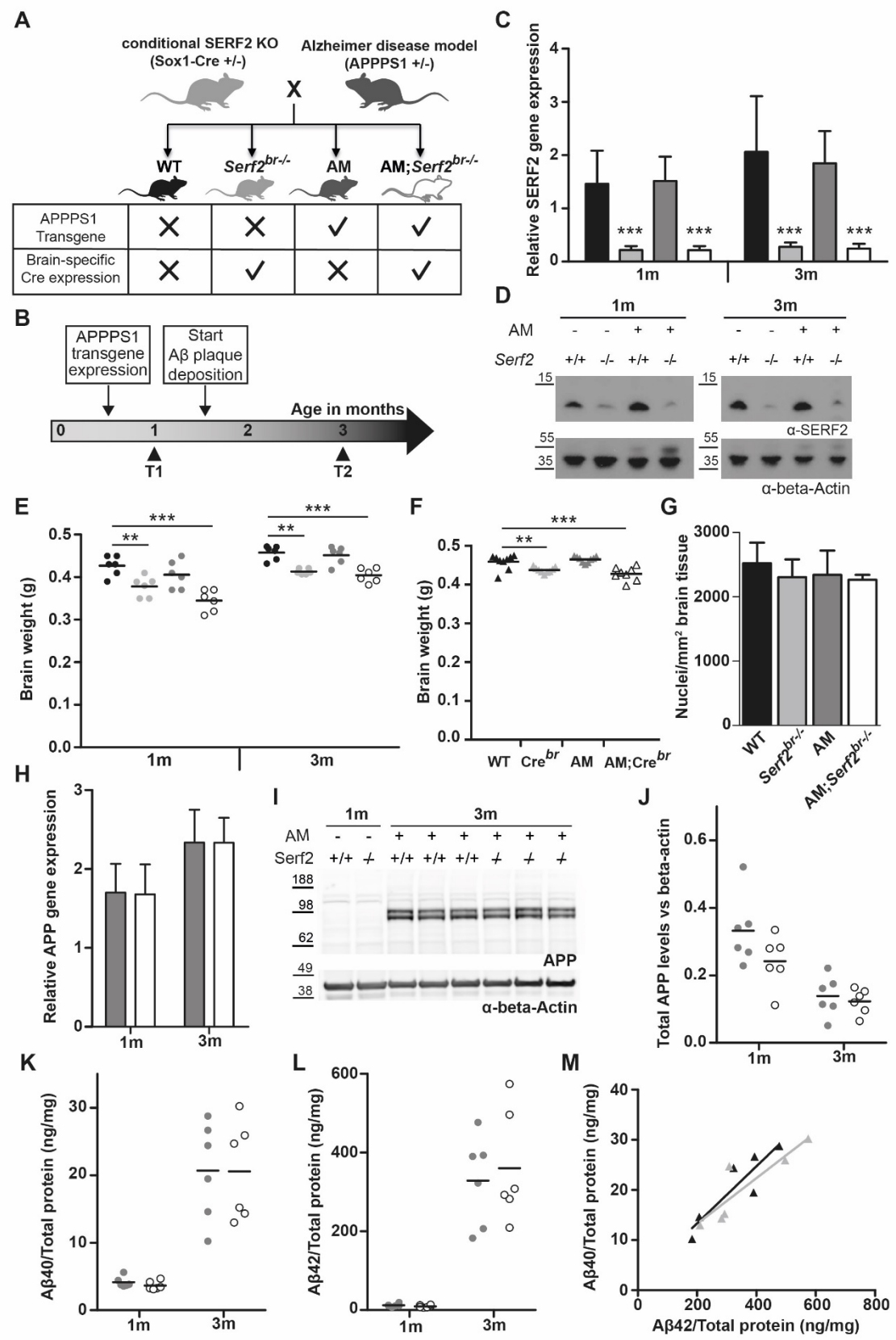
A
conditional SERF2 KO (Sox1-Cre +/-)
Alzheimer disease model (APPPS1 +/-)
X
WT
Serf2br-/-
AM
AM;Serf2br-/-
APPPS1 Transgene
Brain-specific Cre expression
B
APPPS1 transgene expression
Start Aβ plaque deposition
Age in months
T1
T2
C
Relative SERF2 gene expression
1m
3m
D
AM
Serf2
α-SERF2
α-beta-Actin
E
Brain weight (g)
F
Brain weight (g)
WT
Crebr
AM
AM;Crebr
G
Nuclei/mm² brain tissue
H
Relative APP gene expression
I
APP
α-beta-Actin
J
Total APP levels vs beta-actin
K
Aβ40/Total protein (ng/mg)
L
Aβ42/Total protein (ng/mg)
M
Aβ40/Total protein (ng/mg)
Aβ42/Total protein (ng/mg)

Figure 3

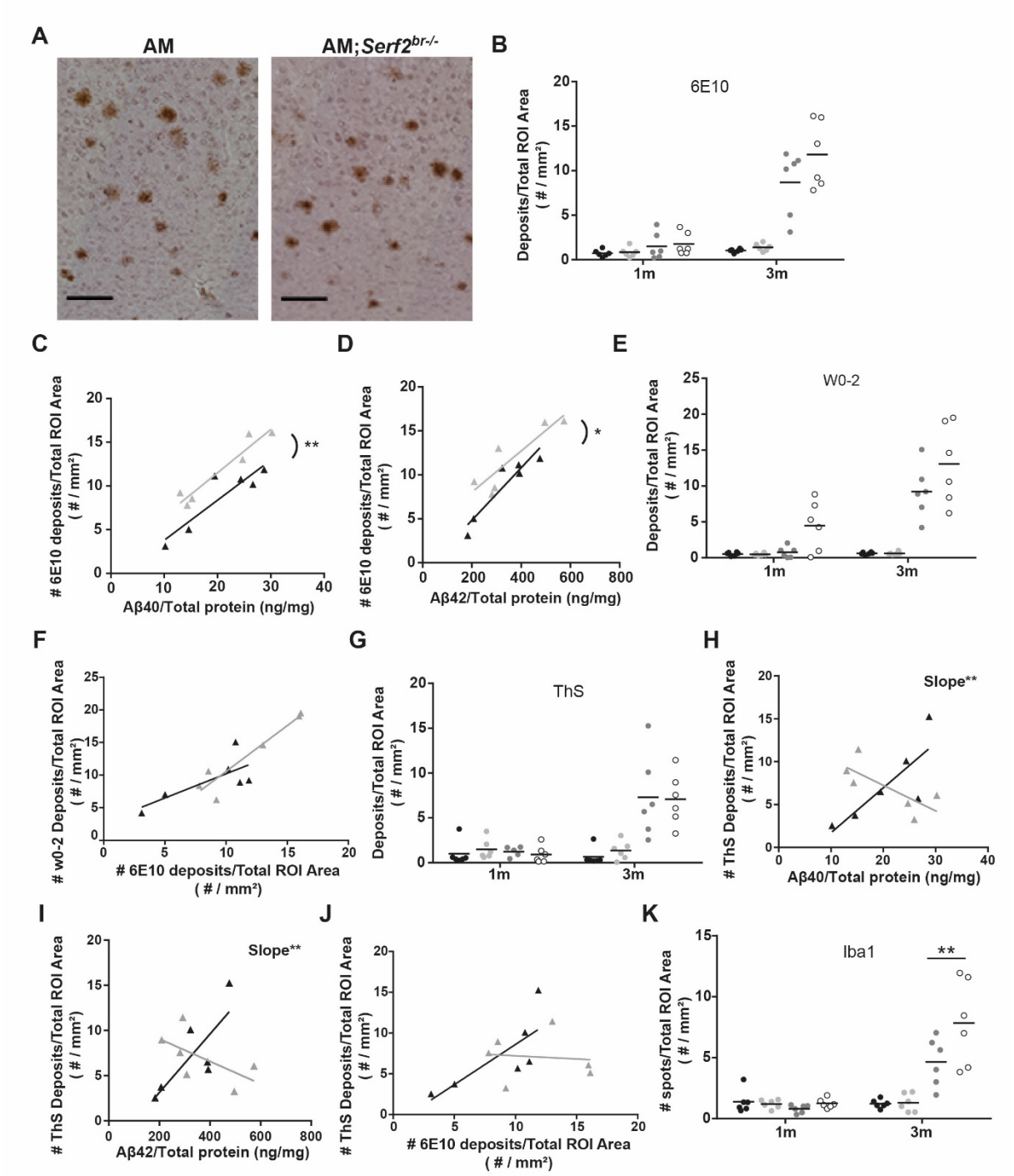
A
AM
AM;Serf2br-/-
B
6E10
Deposits/Total ROI Area (# / mm²)
1m
3m
C
6E10 deposits/Total ROI Area (# / mm²)
Aβ40/Total protein (ng/mg)
**
D
6E10 deposits/Total ROI Area (# / mm²)
Aβ42/Total protein (ng/mg)
*
E
W0-2
Deposits/Total ROI Area (# / mm²)
1m
3m
F
w0-2 Deposits/Total ROI Area (# / mm²)
6E10 deposits/Total ROI Area (# / mm²)
G
ThS
Deposits/Total ROI Area (# / mm²)
1m
3m
H
Slope**
ThS Deposits/Total ROI Area (# / mm²)
Aβ40/Total protein (ng/mg)
I
Slope**
ThS Deposits/Total ROI Area (# / mm²)
Aβ42/Total protein (ng/mg)
J
ThS Deposits/Total ROI Area (# / mm²)
6E10 deposits/Total ROI Area (# / mm²)
K
Iba1
**
spots/Total ROI Area (# / mm²)
1m
3m

Figure 4

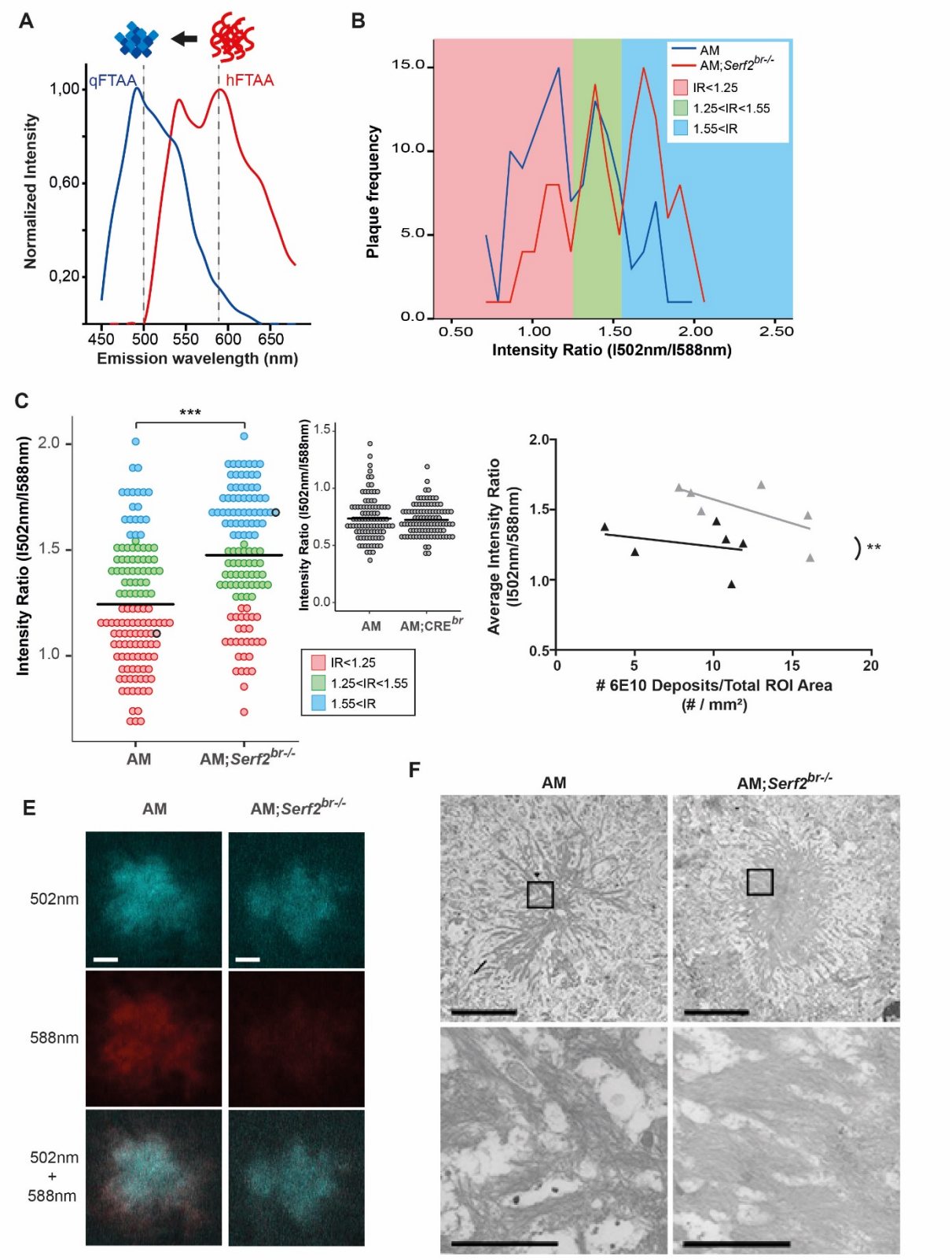
A
qFTAA
hFTAA
Normalized Intensity
1,00
0,60
0,20
450 500 550 600 650
Emission wavelength (nm)
B
AM
AM;Serf2br-/-
IR<1.25
1.25<IR<1.55
1.55<IR
Plaque frequency
15.0
10.0
5.0
0.0
0.50 1.00 1.50 2.00 2.50
Intensity Ratio (I502nm/I588nm)
C
***
Intensity Ratio (I502nm/I588nm)
2.0
1.5
1.0
AM
AM;Serf2br-/-
Intensity Ratio (I502nm/I588nm)
1.5
1.0
0.5
0.0
AM
AM;CREbr
IR<1.25
1.25<IR<1.55
1.55<IR
Average Intensity Ratio (I502nm/I588nm)
2.0
1.5
1.0
0.5
0 5 10 15 20
6E10 Deposits/Total ROI Area (# / mm²)
**
E
AM
AM;Serf2br-/-
502nm
588nm
502nm + 588nm
F
AM
AM;Serf2br-/-

980 **Supplemental figure legends**

981 **Supplemental Figure 1. Additional full-body *Serf2*$^{-/-}$ mice validation and phenotype**
982 **confirmation. (A)** Targeting strategy used to delete exon 2 of *Serf2* by using the 'knockout-first'-
983 allele (adjusted from Skarnes et al. 2011). Top panel: exon/intron structure of *Serf2* including the
984 positions of the LacZ and Neo cassettes, as well as loxP sites. Bottom panel: the *Serf2* allele after
985 recombination events as a result of crosses with *Hprt-Cre* mice. **(B)** Western blot analysis of liver,
986 heart and brain tissue of a *Serf2*$^{+/+}$, *Serf2*$^{+/-}$ and *Serf2*$^{-/-}$ adult mice to detect Serf2 and actin. **(C)** Real
987 time RT-PCR analyses of *Serf2* in different organs of adult mice with the following genotypes *Serf2*$^{+/+}$
988 (n=3), *Serf2*$^{+/-}$ (n=8) and *Serf2*$^{-/-}$ (n=1). *Serf2* levels were normalized to the housekeeping gene 18S
989 (mean ± SEM). **(D)** Lateral view of a *Serf2*$^{-/-}$ and *Serf2*$^{+/-}$ embryo and placenta at embryonic day 15.5
990 and 17.5. **(E)** Weight measurements of *Serf2*$^{+/+}$, *Serf2*$^{+/-}$, *Serf2*$^{-/-}$ embryos at E17.5 and P0 (black line =
991 mean, Two-way ANOVA with factors age and genotype, Bonferroni corrected post-hoc comparison
992 for *Serf2*$^{+/-}$ and *Serf2*$^{-/-}$ compared to *Serf2*$^{-/-}$ *p<0.05; ***p<0.001). **(F)** Hematoxylin and Eosin staining
993 on *Serf2*$^{-/-}$ and *Serf2*$^{+/+}$ lung and kidney tissue at E17.5 (10 times magnification). For all panels:
994 *Serf2*$^{+/+}$= black, *Serf2*$^{+/-}$ = dark grey, *Serf2*$^{-/-}$ = light grey.

995 **Supplemental Figure 2. Cell culture data of *Serf2* KO and control HEK cells and RNA**
996 **sequencing analysis of mouse embryonic fibroblasts (MEFs) isolated from full-body *Serf2*$^{-/-}$ and**
997 **control mice. (A)** Growth curve of two CRISPR-induced *Serf2*$^{-/-}$ clones of HEK293T versus wild-type
998 HEK293T. (Three replicates measured,full line=replicate average, dashed lines=standard deviation on
999 average) **(B)** Network showing the interconnectivity of enriched GO-terms in RNA sequencing data
1000 from *Serf2*$^{-/-}$ and control MEFs. Circle size indicates amount of differentially expressed genes found in
1001 each GO-category. Edges were drawn when the minor category shared more than 25 % of its found
1002 genes with the major category. Edge color indicates the major category in the relationship. Edge
1003 thickness indicates the percentage of found genes shared by the minor category. **(C)** Bar chart
1004 indicating the fold change for each GO-term as determined by DAVID. Brackets indicate the three
1005 main GO-term clusters defined based on the network in (B).

1006 **Supplemental Figure 3. Additional validation of the brain-specific knock-out of *Serf2*. (A)**
1007 Modified targeting strategy used to delete the exon 2 of *Serf2* specifically in the central nervous
1008 system. **(B)** Real time RT-PCR analyses of *Serf2* RNA expression in different organs $Serf2^{+/+}$ and
1009 $Serf2^{br-/-}$ female mice at 1 month and 3 months of age. *Serf2* expression was normalized to
1010 housekeeping gene beta-actin (all groups n=6, mean ± SEM). **(C)** Western blot analysis and
1011 quantification of *Serf2* and beta-actin in brain lysates of WT and $Serf2^{br-/-}$ female mice at 1 month
1012 (both groups n=6, mean ± SEM, t-test **p<0.01). **(D)** Brain weight of unfloxed WT and CRE^{br} mice at
1013 1 and 3 months of age (black line = mean, Two-way ANOVA with factors age and genotype,
1014 Bonferroni corrected post-hoc for CRE^{br} compared to WT *p_{bon}<0.05). **(E)** Evolution of brain weight
1015 in WT and $Serf2^{br-/-}$ female mice between 1 and 11 months of age (black line = mean).

1016 **Supplemental Figure 4. Overview of distribution and general morphological parameters of**
1017 **6E10-stained Aβ deposits in AM and AM;$Serf2^{br-/-}$ mice at 3 months of age. (A)** Light microscope
1018 images of the 6E10 immunostained sagittal section of 3-month-old AM and AM;$Serf2^{br-/-}$ female mice
1019 (scale bar = 1mm, black rectangle = magnified region in main Figure 3). **(B)** Boxplots showing the
1020 distribution of the surface area of the individual plaques measured in AM and AM;$Serf2^{br-/-}$ mice at 3
1021 months of age. **(C)** Boxplots showing the distribution of the circularity of the individual plaques
1022 measured in AM and AM;$Serf2^{br-/-}$ mice at 3 months of age. **(D)** Boxplots showing the distribution of
1023 the solidity of the individual plaques measured in AM and AM;$Serf2^{br-/-}$ mice at 3 months of age. For
1024 all boxplots: black line = median, box = 25th-75th percentile, whiskers = 1.5 x interquartile range
1025 (IQR), circles = outlier value > 1.5x IQR, asterisks = extreme outlier value > 3x IQR.

1026 **Supplemental Figure 5. Overview of distribution and detailed W0-2-stained Aβ deposits in AM**
1027 **and AM;$Serf2^{br-/-}$ mice at 3 months of age.** Light microscope images of the W0-2 immunostained
1028 sagittal section of 3-month-old AM and AM;$Serf2^{br-/-}$ female mice (scale bar = 1mm, black rectangle =
1029 magnified in insert on the right, insert scale bar = 100µm).

1030 **Supplemental Figure 6. Correlation plots illustrating the relationship of different stains in**
1031 **individual mice. (A)** Correlation plot depicting the relationship between the density of 6E10 deposits

1032 and Iba1-positive spots in AM (black) and AM;*Serf2*$^{br-/-}$ (grey) mice at 3 months of age. **(B)**
1033 Correlation plot depicting the relationship between W0-2 plaque density and the LCO average
1034 intensity ratio in AM (black) and AM;*Serf2*$^{br-/-}$ (grey) mice at 3 months of age. **(C)** Correlation plot
1035 depicting the relationship between ThS plaque density and the LCO average intensity ratio in AM
1036 (black) and AM;*Serf2*$^{br-/-}$ (grey) mice at 3 months of age. For all plots: detailed statistics in
1037 Supplemental Table 3; *p <0.05.

1038 **Supplemental Figure 7. Overview and detailed view of Aβ staining pattern after W0-2 and 6E10**
1039 **staining in AM and AM;*Serf2*$^{br-/-}$ mice at 1 month of age. (A)** Light microscope images of the W0-2
1040 immunostained sagittal section of 1-month-old AM and AM;*Serf2*$^{br-/-}$ female mice. **(B)** Light
1041 microscope images of the 6E10 immunostained sagittal section of 1-month-old AM and AM;*Serf2*$^{br-/-}$
1042 female mice. All pictures: main scale bar = 1mm, black rectangle = magnified in insert on the right,
1043 insert scale bar = 100μm.